Geophysical Journal International

Geophys. J. Int. (2010) **181,** 818–846 doi: 10.1111/j.1365-246X.2010.04541.x

Modelling sound propagation in the Southern Ocean to estimate the acoustic impact of seismic research surveys on marine mammals

Monika Breitzke[1,*] and Thomas Bohlen[2]

[1]*Alfred-Wegener-Institute for Polar and Marine Research (AWI), Am Alten Hafen* 26, D-27568 *Bremerhaven, Germany. E-mail: Monika.Breitzke@awi.de*
[2]*Karlsruhe Institute of Technology (KIT), Geophysical Institute, Hertzstraße* 16, D-76187 *Karlsruhe, Germany*

Accepted 2010 January 25. Received 2010 January 9; in original form 2009 October 10

SUMMARY

Modelling sound propagation in the ocean is an essential tool to assess the potential risk of air-gun shots on marine mammals. Based on a 2.5-D finite-difference code a full waveform modelling approach is presented, which determines both sound exposure levels of single shots and cumulative sound exposure levels of multiple shots fired along a seismic line. Band-limited point source approximations of compact air-gun clusters deployed by R/V *Polarstern* in polar regions are used as sound sources. Marine mammals are simulated as static receivers. Applications to deep and shallow water models including constant and depth-dependent sound velocity profiles of the Southern Ocean show dipole-like directivities in case of single shots and tubular cumulative sound exposure level fields beneath the seismic line in case of multiple shots. Compared to a semi-infinite model an incorporation of seafloor reflections enhances the seismically induced noise levels close to the sea surface. Refraction due to sound velocity gradients and sound channelling in near-surface ducts are evident, but affect only low to moderate levels. Hence, exposure zone radii derived for different hearing thresholds are almost independent of the sound velocity structure. With decreasing thresholds radii increase according to a spherical 20 $\log_{10}$ r law in case of single shots and according to a cylindrical 10 $\log_{10}$ r law in case of multiple shots. A doubling of the shot interval diminishes the cumulative sound exposure levels by −3 dB and halves the radii. The ocean bottom properties only slightly affect the radii in shallow waters, if the normal incidence reflection coefficient exceeds 0.2.

Key words: Controlled source seismology; Computational seismology; Wave propagation; Acoustic properties; Antarctica.

1 INTRODUCTION

Modelling sound propagation in the ocean is a well-established method to predict traveltimes and mode shapes of acoustic waves propagated along long ranges and often geodesic paths. Typical fields of application are the propagation of sound waves in oceanic waveguides (e.g. Urick 1983; Brekhovskikh & Lysanov 2003) and the propagation of earthquake-generated sound waves across ocean basins and in the SOFAR channel (e.g. Blackman *et al.* 2004; Williams *et al.* 2006; de Groot-Hedlin *et al.* 2009). Due to the long propagation ranges the applied methods are often approximations of the full elastic wave equation, which do not include all wave types and wave propagation phenomena. Hence, they often compute only traveltimes correctly but not amplitudes. Commonly used methods are ray tracing, normal mode superposition and parabolic equation (PE) solutions of the wave equation (Jensen *et al.* 2000; Etter 2003). Full waveform solutions like the finite-difference (FD) or finite-element (FE) method, often applied to simulate elastic wave propagation in the solid earth, are not widely used for ocean acoustic problems.

Sound sources are usually implemented as omnidirectional point sources emitting waveforms like the Ricker wavelet (Ricker 1953). This even applies to marine exploration seismology, where wide air-gun arrays of more than 10 m width and lengths (Caldwell & Dragoset 2000; Dragoset 2000) are used. Only Landrø *et al.*'s (1993) study tries to include the directivity of an air-gun array in a coarse FD modelling scheme.

Modelling sound propagation for estimating the acoustic impact of anthropogenic noise on marine mammals is quite new. Only few approaches exist, which include the relevant components with different degrees of accuracy. Various purposes are followed by such modelling studies.

(1) They are used as a planning tool to estimate the acoustic impact of e.g. a seismic survey into a region to predict its potential risk on marine biota in general.

*Now at: Department of Geosciences, University of Bremen, Bibliothekstraße 1, D-28359 Bremen, Germany.

The Effects of Sound on the Marine Environment (ESME) computer model is a very ambitious approach for such purposes (Gisiner *et al.* 2006; Shyu & Hillson 2006). It incorporates different sound sources (Shyu & Hillson 2006), 3-D sound velocity fields in the water column (Linder & Gawarkiewicz 2006; Lynch *et al.* 2006), geoacoustic properties of the seafloor, (Shyu & Hillson 2006), different sound propagation models (Siderius & Porter 2006) and moving marine mammals as receivers (Houser 2006; Shaffer & Costa 2006). However, no application to *in situ* data has been published yet.

Erbe & King (2009) published a less complex, computation-time efficient method, which applies a combined cluster analysis—neural network approach. It also takes the sound velocity profile of the water column and the geoacoustic properties of the seafloor into account, considers the signature and directivity of air-gun arrays (Ziolkowski 1970; Laws *et al.* 1990; Landrø 1992), simulates sound propagation by a combined a ray tracing—PE approach (Collins 1993, 1999) and assumes marine mammals as static receivers. Maps of cumulative sound exposure levels (SELs) emitted into a shallow coral reef off Australia by a grid of seismic lines are presented as example.

However, neither the ESME nor Erbe & King's (2009) method include a full waveform model, so that sound propagation in specific oceanographic features like near-surface ducts or a conversion to Scholte waves (e.g. Bohlen *et al.* 2004; Kugler *et al.* 2005, 2007) in very shallow waters might not be simulated correctly.

(2) Modelling studies are used to complement environmental impact assessments (EIAs) prepared for regulatory bodies in advance of a seismic survey. Sound fields are computed to derive exposure zone radii, within which certain hearing thresholds are exceeded. These radii have to be observed visually and are subject to mitigation measures like shut-down or ramp-up in case a marine mammal enters a critical exposure zone.

Depending on the noise exposure criteria sound fields of single or multiple shots are required. If the 'rms-level criterion' is applied, the rms sound pressure levels (SPLs) of a single shot are sufficient (e.g. National Marine Fisheries Service 2008). According to this criterion received rms levels greater than 180 dB re 1 μPa are likely to have the potential to cause serious behavioural, physiological and hearing effects in cetaceans and should not be exceeded (Level A harassment). Received rms levels greater than 160 dB re 1 μPa possibly lead to behavioural disturbances (Level B harassment). For underwater pinnipeds received rms levels are allowed to be 10 dB higher.

If the recently proposed 'dual criterion' is applied, zero-to-peak (0-p) and rms SPLs of single shots and SELs of single and multiple shots are necessary (Southall *et al.* 2007). According to this criterion cetaceans might be injured or receive a permanent threshold shift (PTS) during seismic surveys, if either the unweighted 0-p SPLs of a single shot exceed 230 dB re 1 μPa or the M-weighted SELs of single or multiple shots exceed 198 dB re 1 μPa^{2}s. Single shots might cause behavioural responses or a temporary threshold shift (TTS), if cetaceans receive either unweighted 0-p SPLs higher than 224 dB or M-weighted SELs higher than 183 dB. Due to the lack of cumulative SEL data for the onset of TTS due to multiple shots Southall *et al.* (2007) propose several rms-level thresholds, which depend on the hearing abilities of low-, mid- and high-frequency cetaceans. For underwater pinnipeds 0-p SPL and SEL thresholds are defined to be 12 dB lower.

Though the dual criterion is based on the current state of knowledge, the rms-level criterion is often still used in EIAs (e.g. National Marine Fisheries Service 2008). These studies usually take the signatures of the individual air guns and the geometry of the air-gun array into account and apply a ray tracing approach for sound propagation modelling, but neglect the sound velocity profile of the water column and interactions with the seafloor (e.g. LGL Ltd. 2008). No full waveform modelling is used for EIAs up to now.

(3) Only few efforts exist to compare sound propagation modelling with *in situ* seismic calibration surveys (Tolstoy *et al.* 2004, 2009; Breitzke *et al.* 2008; Tashmukhambetov *et al.* 2008). For example, by combining seismic source modelling packages with a PE sound propagation modelling approach Tashmukhambetov *et al.* (2008) found a good agreement between measured and modelled waveforms in the low frequency range, but some discrepancies for the higher frequencies. They attribute these discrepancies to high-frequency sound waves trapped in a near-surface duct.

Problems in modelling sound propagation in surface ducts by different PE methods correctly (Porter & Jensen 1993) and the request to include interactions with the ocean bottom accentuate the need for modelling the acoustic impact of seismic surveys with full waveform methods. Therefore, this paper presents a FD modelling study, which investigates sound propagation in the Antarctic Treaty Area. As sound sources single air guns and point source approximations of compact air-gun clusters are used. Source signatures are modelled by the NUCLEUS^{TM} source modelling package [Petroleum Geo Services (PGS)]. The frequency range is limited to 0–256 Hz. As sound propagation model a viscoelastic 2.5-D FD scheme is used (Bohlen 2002). Marine mammals are simulated as static receivers. The survey layout is confined to one seismic line. The ship moves with a constant speed, while air guns are firing with a given shot interval. This is sufficient, because due to the harsh environmental conditions all seismic surveys in the Southern Ocean are conducted as 2-D surveys, which often have the character of reconnaissance surveys with large spacings between seismic lines.

The objectives are (1) to determine the acoustic impact of single and multiple shots fired along a seismic line, (2) to determine time-dependent exposure histories marine mammals receive at different positions and (3) to determine exposure zone radii for different hearing thresholds. The modelling study is part of a risk assessment study on the impact of seismic research surveys on marine mammals in the Antarctic Treaty area prepared by the Alfred-Wegener-Institute for Polar and Marine Research (AWI). It first gives an introduction to the study area. Subsequently, the air-gun configurations commonly used by R/V *Polarstern*, the source signals and the sound propagation modelling approach are described. As results the SEL fields of single and multiple shots and the exposure histories received at different positions are presented for *iso*-velocity models without and with seafloor and for deep and shallow water models of the study area. The shot interval and the reflection coefficient of the seafloor are varied to investigate their influence on the SEL fields and exposure histories. Finally, exposure zone radii are derived for different hearing thresholds. The results are discussed with respect to the frequency-selective ducting ability of the near-surface sound channels in the study area, the validity of the point source approximation, and the potential influence of higher-frequency side lobes on exposure zone radii. Simple regression equations are established, which allow to estimate exposure zone radii without FD modelling.

2 STUDY AREA

The modelling study focuses on those areas in the Southern Ocean, where most of the multichannel seismic (MCS) research activities were conducted with R/V *Polarstern* since it was taken in service

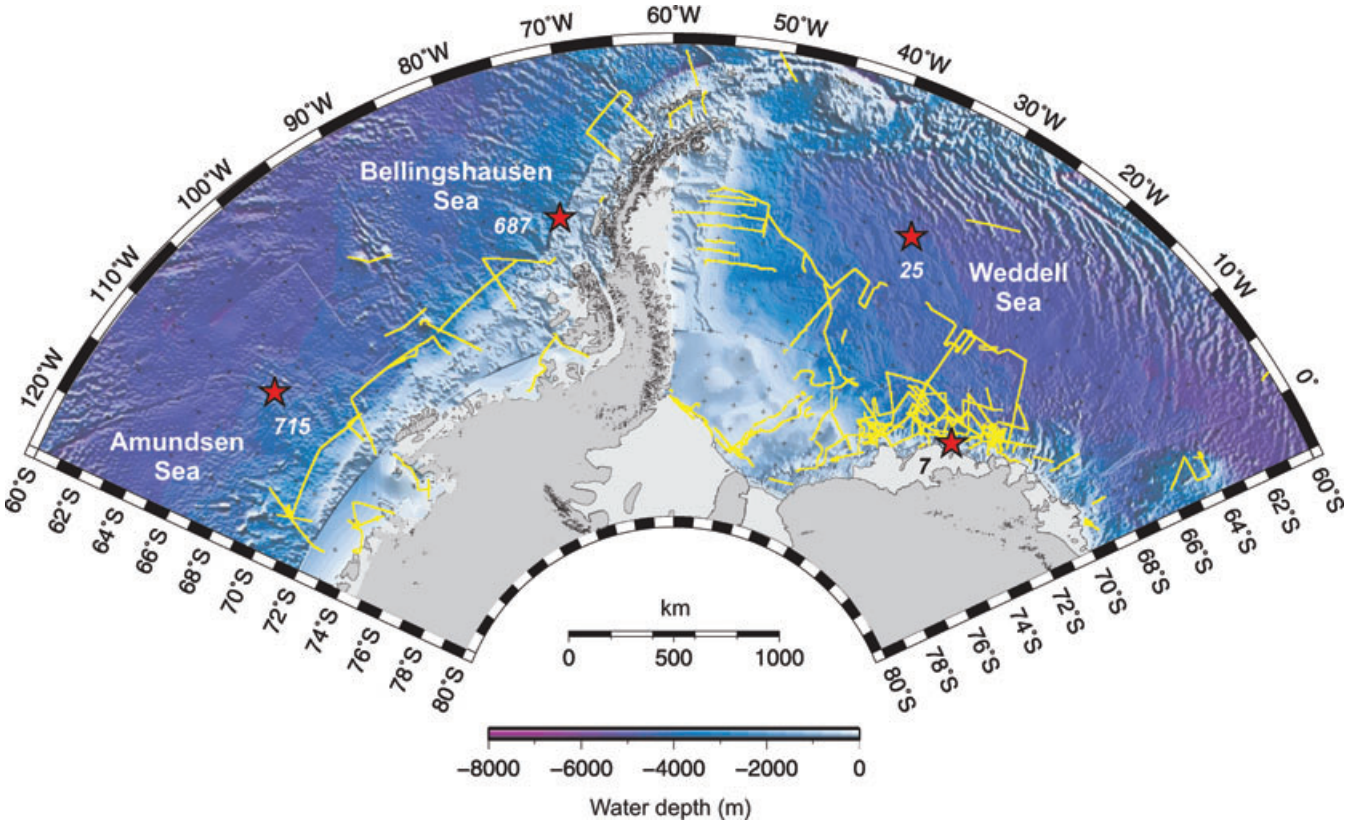

Figure 1. Map of the study area. The track lines of all MCS surveys conducted with R/V *Polarstern* to the Amundsen/Bellingshausen and Weddell Sea since 1982 are superposed in yellow. Red stars mark the positions of the hydrographic stations 715, 687, 25 and 7, from which sound velocity profiles are taken.

in 1982—the Weddell Sea and the Amundsen/Bellingshausen Sea (Fig 1). According to the 'Antarctic Seismic Data Library System for Cooperative Research (SDLS)' (Wardell *et al.* 2007) four MCS cruises took place in the Amundsen/Bellingshausen Sea and ten MCS cruises in the Weddell Sea (Table 1). An analysis of the Julian days indicates, that the main seismic activities were undertaken during the austral summer months from January to March (Figs 2a and b). Histograms of the covered water depths cluster over two maxima, one for shallow to medium waters between ∼200 and ∼1000 m depths and another for deep waters between ∼3000 and

Table 1. Multichannel seismic surveys conducted with R/V *Polarstern* in the Amundsen/Bellingshausen Sea (Marie Byrd Land) and in the Weddell Sea since 1982 (*cf*. Fig. 1).

Cruise	Area	Season	Group	MCS profile length (km)
ANT-IV/3	WS	85/86	BGR	6263
ANT-V/4	WS	86/87	AWI	2800
ANT-VI/2	AP/WS	87/88	AWI/IG Kiel	1400
ANT-VIII/5	WS	89/90	AWI	4100
ANT-VIII/6	WS	89/90	BGR	3213
ANT-X/2	WS	91/92	AWI	3900
ANT-XI/3	AP/MBL	93/94	AWI	3448
ANT-XII/3	WS	94/95	AWI	2000
ANT-XII/4	AP/MBL	94/95	AWI	989
ANT-XIII/3	WS	95/96	AWI	500
ANT-XIV/3	WS	96/97	AWI	4418
ANT-XVIII/5a	AP/MBL	00/01	AWI/VI	572
ANT-XIX/2	AP/WS	01/02	AWI/ING	2930
ANT-XXIII/4	MBL	05/06	AWI/BAS/VI	2227
Total	14 cruises			38 760

Notes: Data are taken from the 'Antarctic Seismic Data Library System for Cooperative Research (SDLS)' (available via http://sdls.ogs.trieste.it), last update at 2009 September 21. WS, Weddell Sea; AP, Antarctic Peninsula; MBL, Marie Byrd Land; BGR, Federal Institute for Geosciences and Resources, Hannover, Germany; AWI, Alfred-Wegener-Institute for Polar- and Marine Research, Bremerhaven, Germany; IG Kiel, Institute for Geophysics, Christian-Albrechts-University, Kiel, Germany; VI, VNIIOkeangeologia, St. Petersburg, Russia; ING, Instituto Nazionale di Oceanografia e di Geofisica Sperimentale, Trieste, Italy; BAS, British Antarctic Survey, Cambridge, UK.

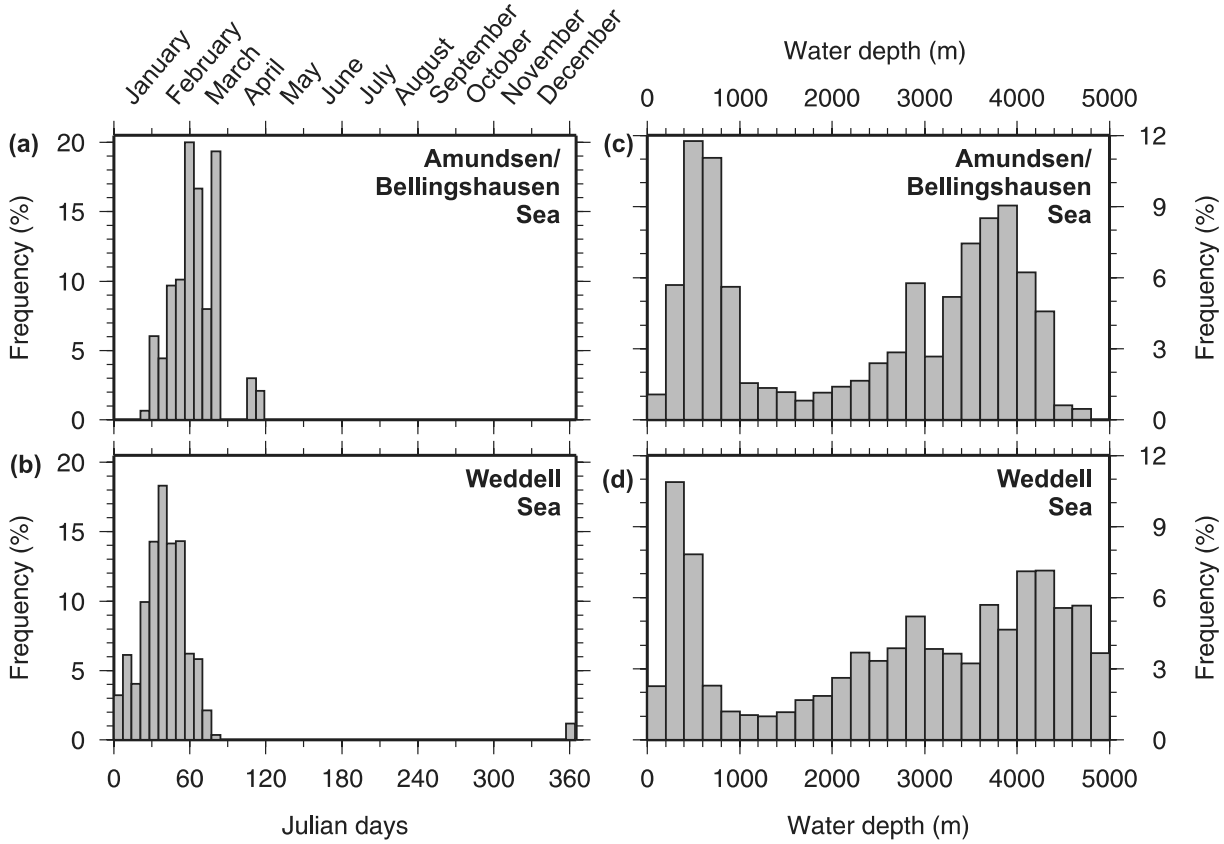

Figure 2. Histograms of the seasonal distribution of the MCS surveys to the Amundsen/Bellingshausen and Weddell Sea and of the water depths covered by the seismic lines. The ordinates of the histograms on the left-hand side (a, b) define the percentage number of shots fired per week (bar width = 7 d) relative to the total number of shots in each area. The ordinates of the histograms on the right-hand side (c, d) define the percentage number of shots fired over water depth ranges of 200 m (= bar width) relative to the total number of shots in each area.

∼4500 m depths (Figs 2c and d). Shallower areas are rarely surveyed, because continental shelves are usually ice-covered.

From a series of oceanographic profiles (Fahrbach *et al.* 2007) four hydrographic (CTD-) stations are selected to derive typical sound velocity profiles for the deep and the shallow/medium water columns (Table 2, Fig. 1). The data of the Amundsen/Bellingshausen Sea—station 715 in the deep sea and station 687 on the continental slope—were collected during February/March and are thus considered to represent typical austral mid-summer conditions (Fig. 3a). The Weddell Sea stations 25 and 7 were collected during March/April and extend the considered time span to the austral spring and fall seasons (Fig. 3b). The sound velocity profiles of the Amundsen/Bellingshausen Sea are characterized by a pronounced sound velocity minimum in ∼80 m depth. Due to the insolation during the summer months this cold, low-velocity channel is overlain by warmer water masses with higher sound velocity. During the austral spring and fall months this higher sound velocity layer is less pronounced, as is indicated by the sound velocity profiles of the Weddell Sea, and vanishes completely towards the austral winter months. Beneath the cold low velocity layer all sound velocity profiles reveal a positive gradient, which increases by ∼15 m s^{-1} per 1000 m.

A compilation of high-resolution seismic, sediment echosounder and sediment core data reveals that the seafloor of the southeastern Weddell Sea is mainly covered by soft sediments (e.g. Kuhn & Weber 1993; Melles & Kuhn 1993; Michels *et al.* 2002). Similar studies in selected regions show that this also applies to the Amundsen/Bellingshausen Sea (e.g. Nitsche *et al.* 2000; Scheuer *et al.* 2006a, b; Dowdeswell *et al.* 2008). Hence, a *P*-wave velocity of 1600 m s^{-1}, a *S*-wave velocity of 330 m s^{-1} and a wet bulk density of 1450 kg m^{-3} are assumed as physical properties of the seafloor (Hamilton 1980; Table 3). Together with an average sound velocity of 1500 m s^{-1} and an average density of 1025 kg m^{-3} for sea water this results in a normal incidence reflection coefficient of

Table 2. Geographical coordinates, water depths and dates of the CTD measurements in the Amundsen/Bellingshausen and the Weddell Sea.

Area	Station number	Longitude	Latitude	Water depth (m)	Date (dd/mm/yy)
AS/BS	715	108°32.76′W	67°00.44′S	4561	04/03/92
AS/BS	687	72°14.22′W	66°43.91′S	2387	24/02/92
WS	25	34°57.72′W	65°49.00′S	4751	09/04/98
WS	7	17°27.66′W	72°11.15′S	2042	30/03/95

Notes: AS/BS, Amundsen/Bellingshausen Sea and WS, Weddell Sea.

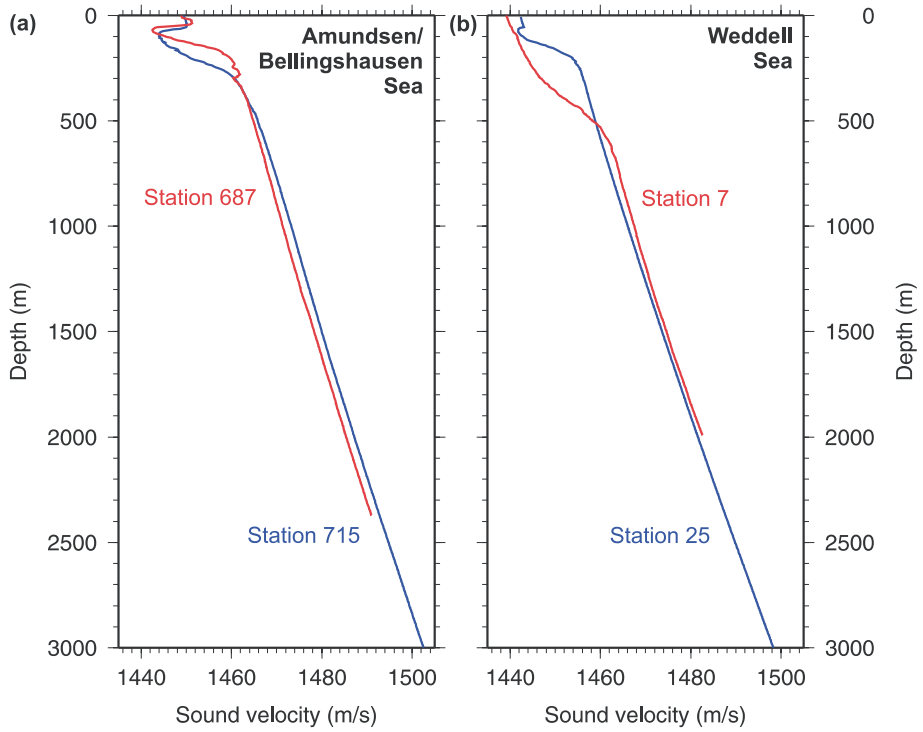

Figure 3. Sound velocity profiles derived from CTD measurements at hydrographic stations 715 and 687 in the Amundsen/Bellingshausen Sea (a) and 25 and 7 in the Weddell Sea (b).

Table 3. Physical properties of the seafloor, critical angles and half critical distances on the seafloor.

V_P (m s^{-1})	V_S (m s^{-1})	ρ (kg m^{-3})	Q_P	Q_S	R	α_{crit} (°)	$x_{crit,3000}/2$ (m)	$x_{crit,400}/2$ (m)
1510	110	1250	1.5×10^6	1.5×10^6	0.1	83.4	25 938	3458
1600	330	1450	1.5×10^6	1.5×10^6	0.2	69.6	8082	1078
1670	400	1710	1.5×10^6	1.5×10^6	0.3	63.9	6130	817
1870	510	1930	1.5×10^6	1.5×10^6	0.4	53.3	4030	537

Notes: The normal incidence reflection coefficient R at the seafloor and the critical angle are computed for a P-wave velocity of 1500 m s^{-1} and a density of 1025 kg m^{-3} of sea water. The half critical distances are computed from the critical angles for 3000 m ($x_{crit,3000}/2$) and 400 m ($x_{crit,400}/2$) water depth. V_P is the P-wave velocity, V_S is the S-wave velocity, ρ is the wet bulk density, Q_P is P-wave quality factor, Q_S is S-wave quality factor, R is the normal incidence reflection coefficient at the seafloor, α_{crit} is the critical angle at the seafloor, $x_{crit,3000}$ is the critical distance for 3000 m water depth, $x_{crit,400}$ is the critical distance for 400 m water depth.

0.2 at the seafloor. Attenuation of P and S waves is neglected, that is, quality factor factors of 1.5×10^6 are assumed.

Based on these parameters and with respect to computation time water depths of 3000 and 400 m are selected for all deep and all shallow water models (Table 4). The sea surface is modelled by a reflection coefficient of -1.0. In the Weddell Sea models the physical properties of the seafloor are varied, so that the reflection coefficient ranges from 0.1 to 0.4 (Table 4).

3 MODELLING APPROACH

The approach consists of three steps: (1) modelling the seismic source, (2) modelling sound propagation in the ocean generated by a single shot and (3) modelling cumulative SELs due to multiple shots fired along a seismic line and exposure histories received by marine mammals.

Table 4. Numerical models.

Model	Water depth (m)	R
Semi-infinite *iso*-velocity model	∞	–
Deep water *iso*-velocity model	3000	0.2
Shallow water *iso*-velocity model	400	0.2
Amundsen/Bellingshausen Sea 715	3000	0.2
Amundsen/Bellingshausen Sea 687	400	0.2
Weddell Sea 25	3000	0.1, 0.2, 0.3, 0.4
Weddell Sea 7	400	0.1, 0.2, 0.3, 0.4

Notes: For the *iso*-velocity models a P-wave velocity of 1500 m s^{-1}, a density of 1025 kg m^{-3} and a P-wave quality factor of 1.5×10^6 is used for sea water. The corresponding S-wave velocity and quality factor are set to 1.0×10^{-6} m s^{-1} and 1.5×10^6, respectively to ensure numerical stability. The numbers behind the Amundsen/Bellingshausen and Weddell Sea models indicate the hydrographic station. R = normal incidence reflection coefficient at the seafloor.

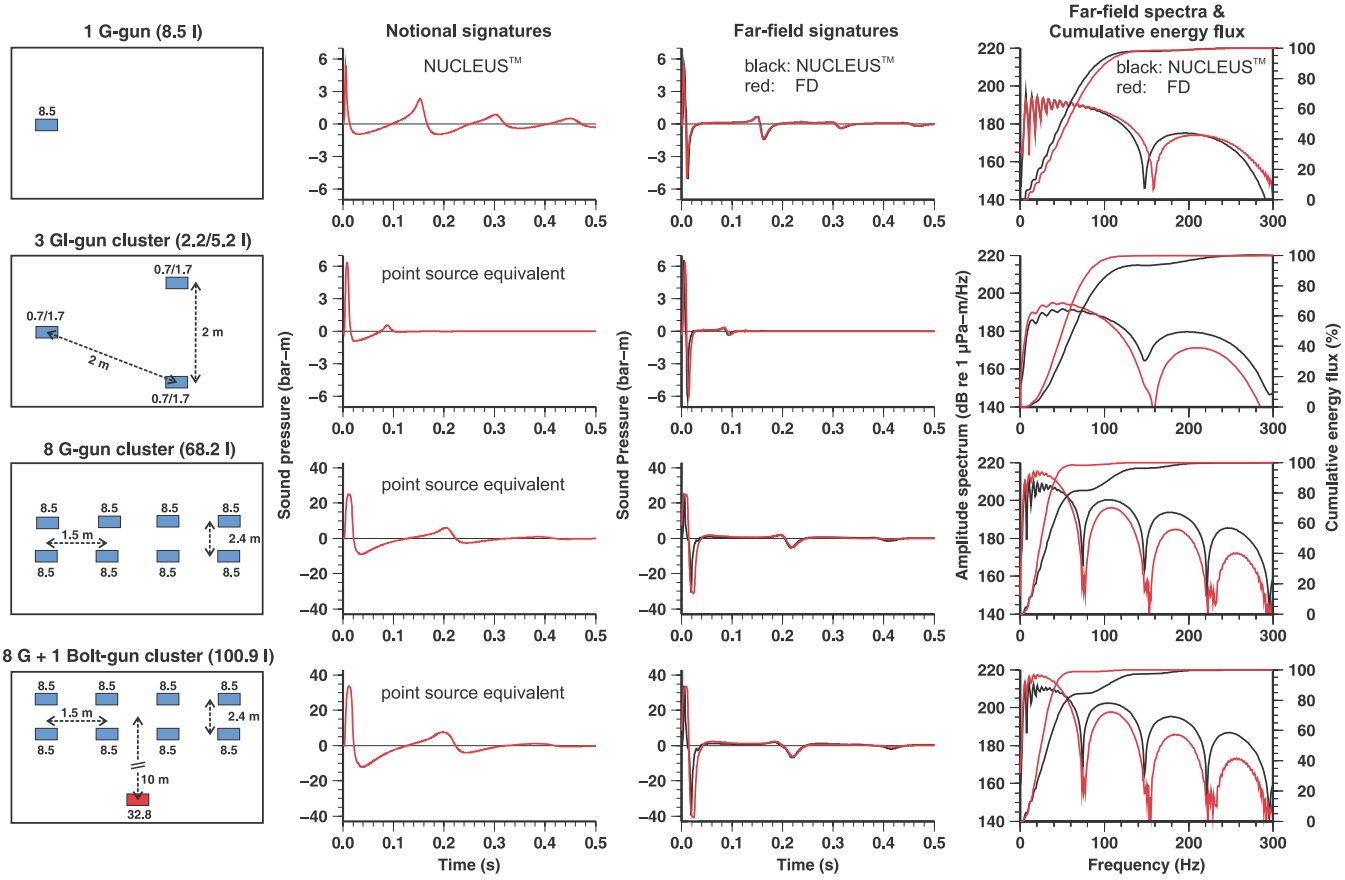

Figure 4. Geometry (not to scale), notional signatures, far-field signatures, far-field spectra and cumulative energy fluxes of the 1 G-gun (row 1), the 3 GI-gun cluster (row 2), the 8 G-gun cluster (row 3) and the 8 G + 1 Bolt-gun cluster (row 4). The notional signatures are either computed by the NUCLEUS™ software or result from an integration of the NUCLEUS™ far-field signature and represent the notional signature of the point source equivalent of the air-gun cluster. The source signatures computed by the NUCLEUS™ software for the exact cluster geometry (black) and derived from the semi-infinite FD model for the point source equivalents (red) are compared in columns 3 and 4.

3.1 Modelling the seismic source

Four air-gun configurations used by R/V *Polarstern* for seismic research surveys in polar regions are considered: a 1 G gun, a 3 GI-gun cluster, an 8 G-gun cluster, and an 8 G + 1 Bolt-gun cluster (Fig. 4).

The 1 G gun has a total volume of 8.5 l. The 3 GI-gun cluster has a triangular, equilateral geometry with 2 m side length and two guns facing the ship stern. Each GI gun has a generator/injector volume of 0.7/1.7 l and is operated in 'True GI' mode (Landrø 1992). Both configurations are towed in 5 m depth, fired every 10 s and used for high-resolution seismic reflection surveys.

The 8 G-gun cluster consists of two parallel substrings with four G guns each towed inline. G-gun spacing inline is 1.5 m, substring spacing crossline 2.4 m. Each G gun has a volume of 8.5 l. The cluster is towed in 10 m depth, fired every 15 s and used for deep crustal seismic reflection surveys.

The 8 G + 1 Bolt-gun cluster consists of the 8 G-gun cluster described above plus a Bolt 1500 LL gun with 32.8 l volume. The 8 G-gun cluster is towed at the starboard side and the Bolt gun at the portside of the ship (or vice versa), so that they have a lateral spacing of 10 m. This configuration is also towed in 10 m depth, fired every 60 s and used for deep crustal seismic refraction and wide-angle reflection surveys.

Compared to the wide air-gun arrays used in exploration seismology with more than 20 m width and 10 m length (e.g. Caldwell & Dragoset 2000; Dragoset 2000) the air-gun clusters considered here for surveys in polar regions have a compact geometry, so that in practice they can be towed in the ice-free channel behind the vessel (Jokat *et al.* 1995).

The acoustic pressure waveforms of the individual air guns (notional signatures) and the far-field signatures of the air-gun clusters are computed by the NUCLEUS™ source modelling package (PGS). It is essentially based on the physics of oscillating spherical bubbles in water, takes interactions of adjacent, closely spaced air guns into account, considers a reflection coefficient at the sea surface of ~ -1.0 for the computation of the far-field signature and is calibrated for the downward directed sound emission (Ziolkowski 1970; Ziolkowski *et al.* 1982). The maximum frequency, which can be considered, is 1 kHz. Several optional filters allow limiting the bandwidth. In this study, we use a DFS-V bandpass filter with 256 kHz high-cut frequency and 72 dB/octave filter slope.

These modelled pressure waveforms are used as source signals in a 2.5-D FD code. As this FD code implies azimuthal symmetry (*cf*. Section 3.2) only point sources located on the cylinder axis ($r = 0$) or ring sources around the cylinder axis ($r \neq 0$) can be simulated. Therefore, the compact air-gun clusters have to be approximated by 'point source equivalents', so that the source signal characteristics

of the air-gun clusters are preserved as far as possible. To realize this requirement the following approach is applied.

(1) In the case of a single air gun the notional signature $n(t)$ computed by the NUCLEUS^{TM} software is used as source signal (Fig. 4).

(2) In the case of the compact air-gun clusters the time-integrated far-field signature $f(t)$ computed by the NUCLEUS^{TM} software is used as source signal $\tilde{n}(t) = \int f(t)dt$. $\tilde{n}(t)$ resembles a notional signature and approximately includes the characteristics of the signal emitted by the air-gun cluster vertically downwards (Fig. 4). This approach is justified, because the superposition of the notional signature $n(t)$ and its time-delayed sea surface reflection $-n(t - 2h/v)$ approximately results in a differentiated notional signature $\tilde{n}'(t)$, which can be measured as far-field signature $f(t)$ vertically beneath the source. That is, $n(t) - n(t - 2h/v) \approx f(t) \approx \tilde{n}'(t)$, where h is the source depth and v is the sound velocity in sea water. How exact this differentiation actually meets the far-field signature or, how closely the integration of the far-field signature resembles the notional signature depends on how short the time $t = 2h/v$ is compared to the dominant period of the notional signature.

This point source approximation neglects the downward focusing effect of the air-gun cluster geometry and uses the maximum signal emitted vertically downwards as source signal. This implies that the energy emitted by the point source equivalents in non-vertical directions is somewhat higher than the energy actually emitted by the air-gun clusters. Therefore, all ranges and exposure zone radii derived in the subsequent sections are upper limits. A detailed discussion on the range of validity of the point source approximation is given in Section 5.2.

3.2 Modelling sound propagation in the ocean (single shots)

A viscoelastic 2.5-D FD code is used for a full waveform modelling of sound propagation in the ocean (Bohlen 2002). It is based on cylinder coordinates, uses 4th order operators and implies an azimuthal symmetry of the 2-D input model. Reflections from the model boundaries are attenuated by exponentially damping layers (Cerjan *et al.* 1985). In contrast to 2-D FD models this 2.5-D code allows to simulate the spherical $1/r$ amplitude decay of point sources in an infinite *iso*-velocity model correctly, whereas 2-D FD models automatically imply line sources with cylindrical $1/\sqrt{r}$ amplitude decay. Thus, if the source directivity and the model parameters have an azimuthal symmetry, the 2.5-D model simulates sound propagation like a 3-D model but with the computation time of a 2-D model.

To determine the SPL and SEL fields of a single shot the following approach is applied.

(1) Synthetic FD seismograms are computed for a dense grid of receiver positions distributed equidistantly over the model in the x–z plane using the notional signatures of the point source equivalents as source signals.

(2) The synthetic seismograms primarily have 'arbitrary' amplitudes, which depend on the FD grid point spacing. Therefore, a rescaling is necessary. This is achieved by running the semi-infinite *iso*-velocity model once for each air-gun cluster. From the peak-to-peak amplitude of the far-field signature computed for 1000 m depth vertically beneath the source a scaling factor is derived for each air-gun cluster, so that the rescaled, backcalculated source level ($SL_{p\text{-}p}$) agrees with the $SL_{p\text{-}p}$ of the far-field signature computed by the NUCLEUS^{TM} software for 1 m reference distance (Table 5). This scaling factor is applied to all synthetic seismograms computed for the air-gun cluster.

(3) From the rescaled seismograms maximum 0-p and rms SPLs and SELs are derived. An averaging window length of 200 ms is chosen for the computation of the rms SPLs, because this window length is often considered to be the integration time of mammalian ears for received SPLs. SELs are determined by an integration of the squared pressure amplitudes $p(t)$ of each seismogram over its total duration T according to

$$SEL = 10 \log_{10} \int_0^T p^2(t)dt / 1\ \mu\text{Pa}^2\text{s}.$$

Maximum 0-p SPLs are also derived from the total seismogram duration. The results are 2-D (x–z) SPL and SEL grids, which reflect the sound pressure and sound energy distribution of a single shot.

Table 5. Data acquisition parameters and source signal characteristics of the air-gun configurations.

Air-gun configurations	Total volume[a] (l)	Pressure ($\times 10^5$ Pa)	Shot interval (s)	Towing depth (m)	$SL_{p\text{-}p}$ (dB)[d]	$SL_{0\text{-}p}$ (dB)[d]	SL_{SE} (dB)[e]	P/B ratio
1 G gun	8.5	140	10	5	240	235	213 (213)	5.0
3 G(I)-gun cluster (True-GI mode)[b]	2.2/5.2[c]	190	10	5	242	236	213 (215)	18.0
8 G-gun cluster	68.2	140	15, 30, 60	10	255	249	227 (232)	7.9
8 G-gun cluster + 1 Bolt 1500 LL	100.9	140	60	10	258	251	230 (235)	8.6

Notes: The peak-to-peak and zero-to-peak source levels in columns 6, 7 and the sound exposure source levels in front of the parentheses in column 8 are derived from the far-field signatures computed by the NUCLEUS^{TM} source modelling package. The sound exposure source levels in parentheses in column 8 are determined from the backcalculated far-field signatures computed by the semi-infinite *iso*-velocity FD model 1000 m vertically beneath the source, having used the notional signatures of the point source equivalents as source signals. $SL_{p\text{-}p}$ = peak-to-peak source level; $SL_{0\text{-}p}$ = zero-to-peak source level; SL_{SE} = sound exposure source level; P/B ratio = primary-to-bubble ratio.

[a]The original manufacturer-given volumes of the single air guns are in cubic inches. From these single air gun volumes total volumes are computed in cubic inches, converted to litres and rounded to one decimal digit.

[b]The 3 GI-gun cluster is approximated by an 'equivalent' 3 G-gun cluster with the same total volume (2.2 l) as the generators of the 3 GI guns, because GI guns are not available in the NUCLEUS^{TM} software. The bubble signal is exponentially tapered to a P/B ratio of 18 to approximate the far-field signature of the 3 GI-gun cluster.

[c]Total generator/injector volumes of the 3 GI-gun cluster (7.4 l total volume).

[d]Peak-to-peak and zero-to-peak source level in dB re 1 μPa at 1 m.

[e]Sound exposure source level in dB re 1 μPa^{2}s at 1 m.

The FD computations are run with a grid point spacing of 0.5 m and a sample interval of 0.1 ms to ensure numerical stability and minimize grid dispersion (Bohlen 2002). The seismograms are stored on a 25 m × 25 m grid with a sample interval of 0.5 ms resulting in a Nyquist frequency of 1 kHz. Seismogram durations are 16 s for all deep and 9 s for all shallow water models, so that at least two multiple reflections are included. The sediment thickness is 1 km, the seismic profile length 10 km. Reflections from the model boundaries are attenuated by an exponentially damping frame of 1 km width. Thus, all deep-water models have a size of 11 km × 5 km and all shallow water models a size of 11 km × 2.4 km. On AWI's massively parallel high-performance vector computer NEC-SX8 the average computation times were ∼13.5 hr for the deep and ∼11.5 hr for the shallow water models.

3.3 Modelling cumulative SELs and exposure histories (multiple shots)

To calculate the cumulative acoustic impact of multiple shots 3-D SEL fields of single shots moving along the seismic line with a predefined ship speed and fired with a given shot interval have to be superposed. Therefore, first the 2-D (x–z) SEL grid is extrapolated to the y-direction by rotating it around the cylinder axis and interpolating the resulting values to an equidistant 3-D (x–y–z) grid. Subsequently, assuming plane horizontal layers the 3-D SEL grid is shifted along the seismic line according to the ship speed and shot interval to simulate the second, third, fourth, etc. shot. Finally, the SELs of the shifted grids are added at each grid point to get the 3-D cumulative SELs of multiple shots. In addition, for fixed receiver positions time-dependent exposure histories are extracted.

4 RESULTS

The modelling approach is applied to 13 different model configurations (Table 4) to study the following key questions.

(1) How do multiple shots affect the cumulative SELs?
(2) How do reflections from the seafloor affect the SPLs and SELs?

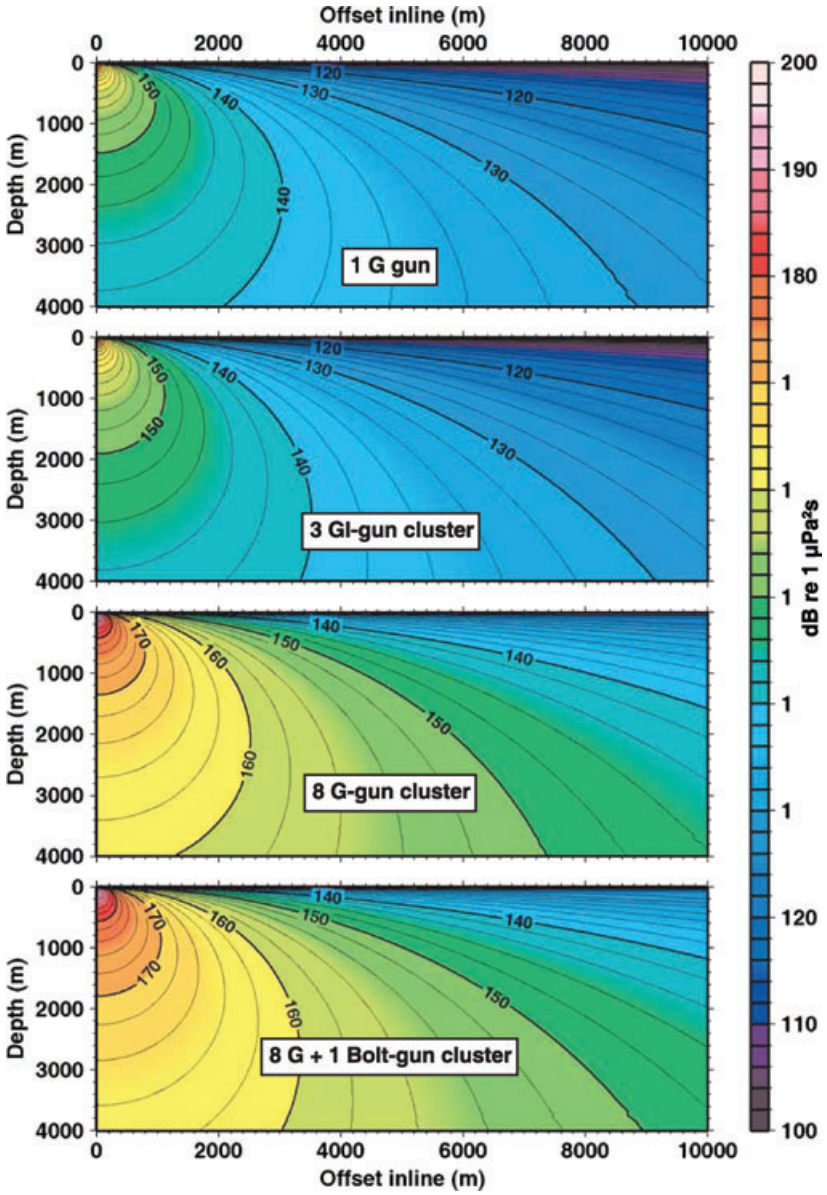

Figure 5. Semi-infinite *iso*-velocity model. SEL inline-depth sections generated by a single shot of the four air-gun configurations.

(3) How does the water depth affect the SPLs and SELs?
(4) How do the sound velocity profiles of the water column affect the SPLs and SELs?
(5) How do changes in the seafloor reflection coefficient affect the SPLs and SELs?
(6) How do exposure histories received by static marine mammals vary between different receiver positions?
(7) How does the shot interval influence the cumulative SELs?
(8) How do the maximum acoustic impacts of the four air-gun configurations differ?

4.1 Semi-infinite *iso*-velocity model

First, the semi-infinite model is used to illustrate the quality of the point source approximation for the downward sound emission. For that, the backcalculated rescaled far-field signatures, far-field spectra and cumulative energy fluxes computed by the FD model and by the NUCLEUS^{TM} software are compared (Fig. 4). In case of the 1 G gun the curves agree almost completely within the considered bandwidth (0–256 Hz). A slight shift in the frequencies of the spectral minima can be attributed to the FD scheme (Virieux 1986; Levander 1988; Bohlen 2002). In case of the compact air-gun clusters spectral amplitudes above ∼100 Hz are slightly reduced due to the integration of the NUCLEUS^{TM} far-field signatures. Hence, 100% of the total energy flux is reached at lower frequencies as in the NUCLEUS^{TM} far-field spectra. In the time-domain the lower frequency content is noticeable by slightly broadened primary signals, which leads to 0–5 dB higher sound exposure source levels (SL_{SE}) than for the NUCLEUS^{TM} far-field signatures (Table 5). Otherwise NUCLEUS^{TM} and FD far-field signatures agree quite well for the downward sound emission.

Second, the semi-infinite model is used to illustrate, that the areas ensonified with certain SELs by a single shot are much greater, if the 8 G- and 8 G + 1 Bolt-gun clusters are used as sound sources as if the 1 G gun and the 3 GI-gun cluster are applied (Fig. 5).

Third, the semi-infinite model is used to illustrate the computation of cumulative SELs and exposure histories from single shots moving along the seismic line. As example, here and in the following sections the 8 G gun cluster is used as sound source firing at intervals of 15 s.

The SEL inline- and crossline-depth sections of the shots 1, 121 and 241 show the typical dipole-like directivity of point sources with highest levels close to the source and almost vanishing levels close to the sea surface (Lloyd mirror effect; Fig. 6). Due to the azimuthal symmetry the inline- and crossline-depth sections agree. Accordingly, the horizontal sections display circular footprints. Their SELs depend on the depth below the sea surface. In 80 m depth SELs are quite low, but increase with greater depths.

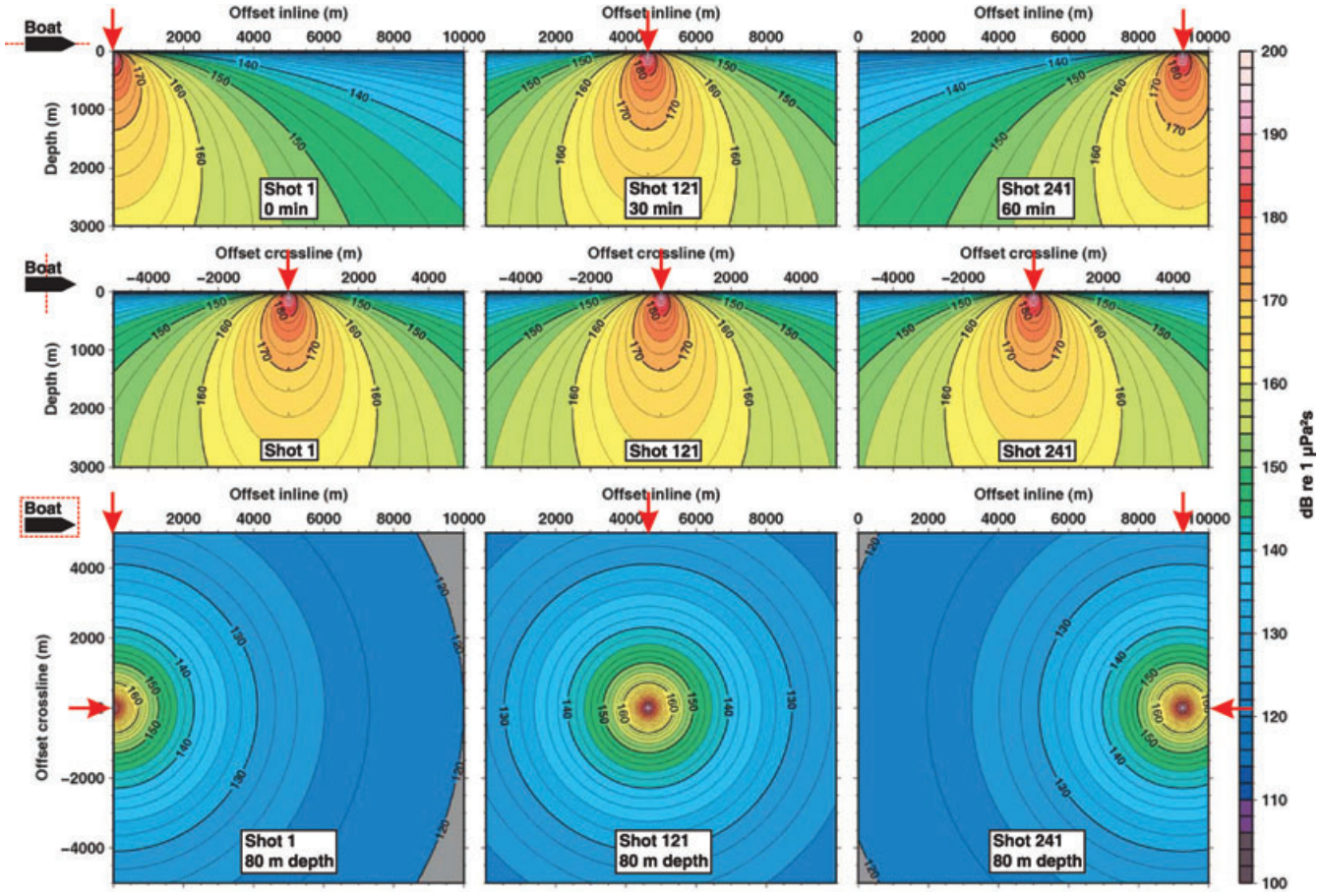

Figure 6. Semi-infinite *iso*-velocity model. SEL inline- and crossline-depth sections (rows 1, 2) and horizontal section 80 m below the sea surface (row 3) generated by a single shot of the eight G-gun cluster. Columns 1, 2 and 3 display the SEL fields of shots 1, 121 and 241 fired after 0, 30 and 60 min survey time at 0, 4630 and 9260 m offset inline. The red arrows mark the position of the ship.

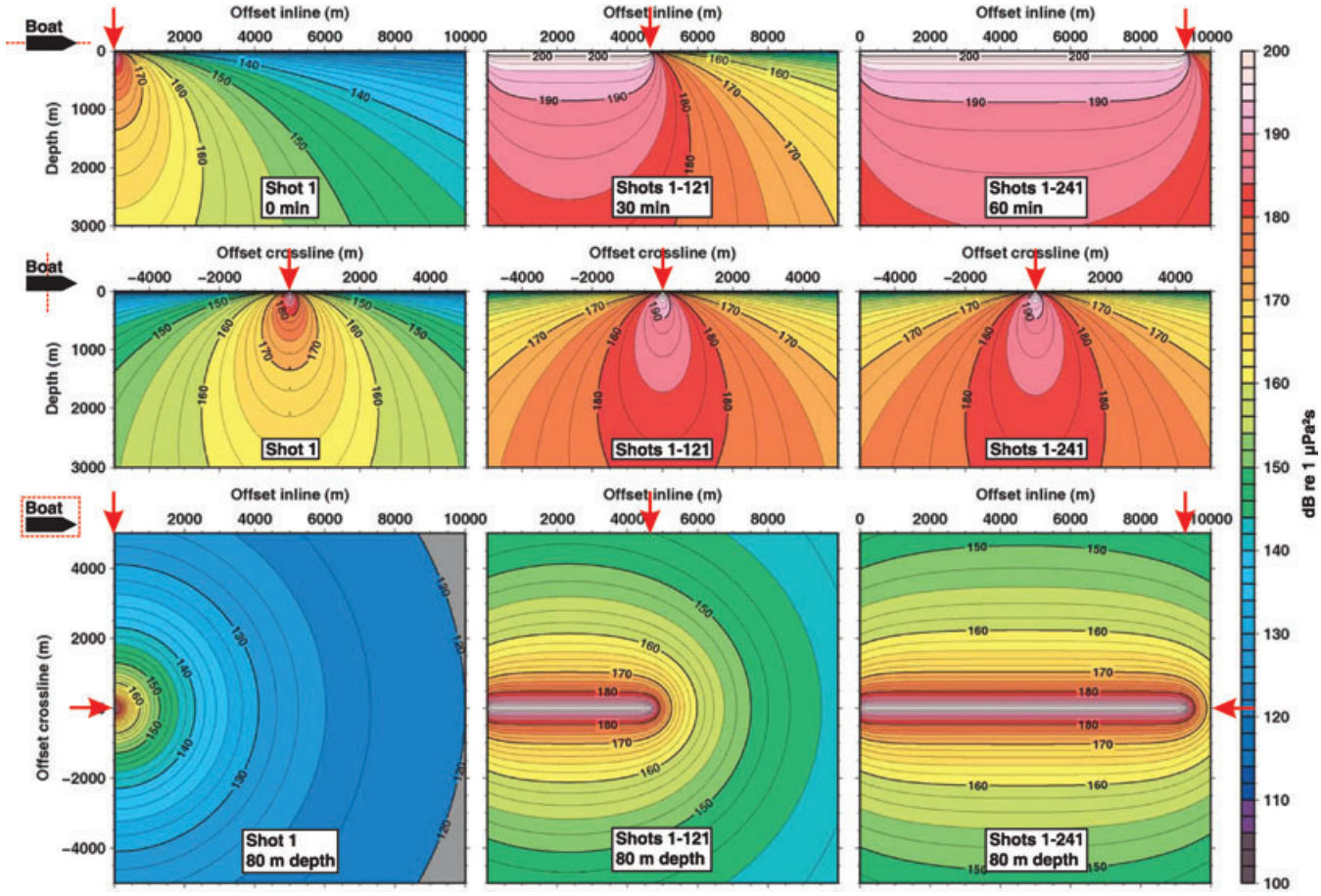

Figure 7. Semi-infinite *iso*-velocity model. Cumulative SEL inline- and crossline-depth sections (rows 1, 2) and horizontal section 80 m below the sea surface (row 3) generated by multiple shots of the 8 G-gun cluster. Columns 1, 2 and 3 display the cumulative SEL fields of 1, 121 and 241 shots after 0, 30 and 60 min survey time, when the ship is located at 0, 4630 and 9260 m offset inline. The red arrows mark the position of the ship.

A successive computation of the cumulative SELs from the moving air-gun shots reveals that a tubular structure of increased SELs develops behind the ship with highest levels vertically beneath the seismic line (Fig. 7). After 30 min survey time the cumulative SELs extend laterally to the ship position at 4630 m offset inline, whereas the dipole-like directivity is preserved crossline, but with higher levels than for a single shot. Accordingly, the horizontal section shows elliptical contour lines with high levels (e.g. >180 dB) confined to the close vicinity of the seismic line. After 60 min survey time the pictures have changed, such that the contour lines inline extend laterally to the new ship position at 9260 m offset. However the depths, where high cumulative SELs occur, are almost the same as after 30 min survey time. Similarly, the cumulative SELs have not increased significantly crossline. Hence, the elliptical contour lines in the horizontal section also extend to the new ship position at 9260 m offset inline, and high levels still concentrate on the area close to the seismic line.

To illustrate the temporal evolution of exposure histories received at different positions it is assumed, that marine mammal stay at 5000 m offset inline, 0, 25, 100, 300, 500 and 1000 m offset crossline and in 5, 80, 380 and 1005 m depth (Fig. 8). If the firing air gun approaches an animal, the 0-p SPLs and SELs received from single shots increase, are highest, if the air gun is directly above the animal, and decrease again during the ship's departure. The exposure histories received from multiple shots first slowly increase, while the ship is approaching. The main impact comes from the air-gun shot(s) directly above the animal leading to a rapid increase in the cumulative SELs. This marks the onset of a plateau, as the contribution of the decreasing levels of the single shots during the ship's departure do not enhance the cumulative SELs significantly on the dB scale.

In 5 and 80 m depth the SELs received from single and multiple shots strongly depend on the animal's offset crossline. With increasing depth the curves approach each other. Though the $SL_{0\text{-}p}$ is 249 dB, the 230 and 224 dB thresholds (0-p) for PTS and TTS in cetaceans due to a single shot—defined by the dual criterion (*cf*. Section 1)—are never exceeded, because no shot position exactly agrees with the animal's position. Similarly, the single shot SEL curves only exceed the 198 dB threshold for PTS in 5 m depth and 0 m offset crossline, that is, if the ship strikes the animal. The 183 dB threshold for TTS is exceeded, if the animals stays either in 5 m depth and 0–25 m offset crossline or in 80 m depth and 0–100 m offset crossline. In case of multiple shots the plateau exceeds the PTS threshold, if the animal stays either in 5 m depth and 0 m offset crossline or in 80 m depth and 0–25 m offset crossline. Especially these latter curves demonstrate that even if single shots do not cause PTS, exposure to multiple rather high-energy shots, which cause TTS, can lead to PTS. In addition, it is worth to note,

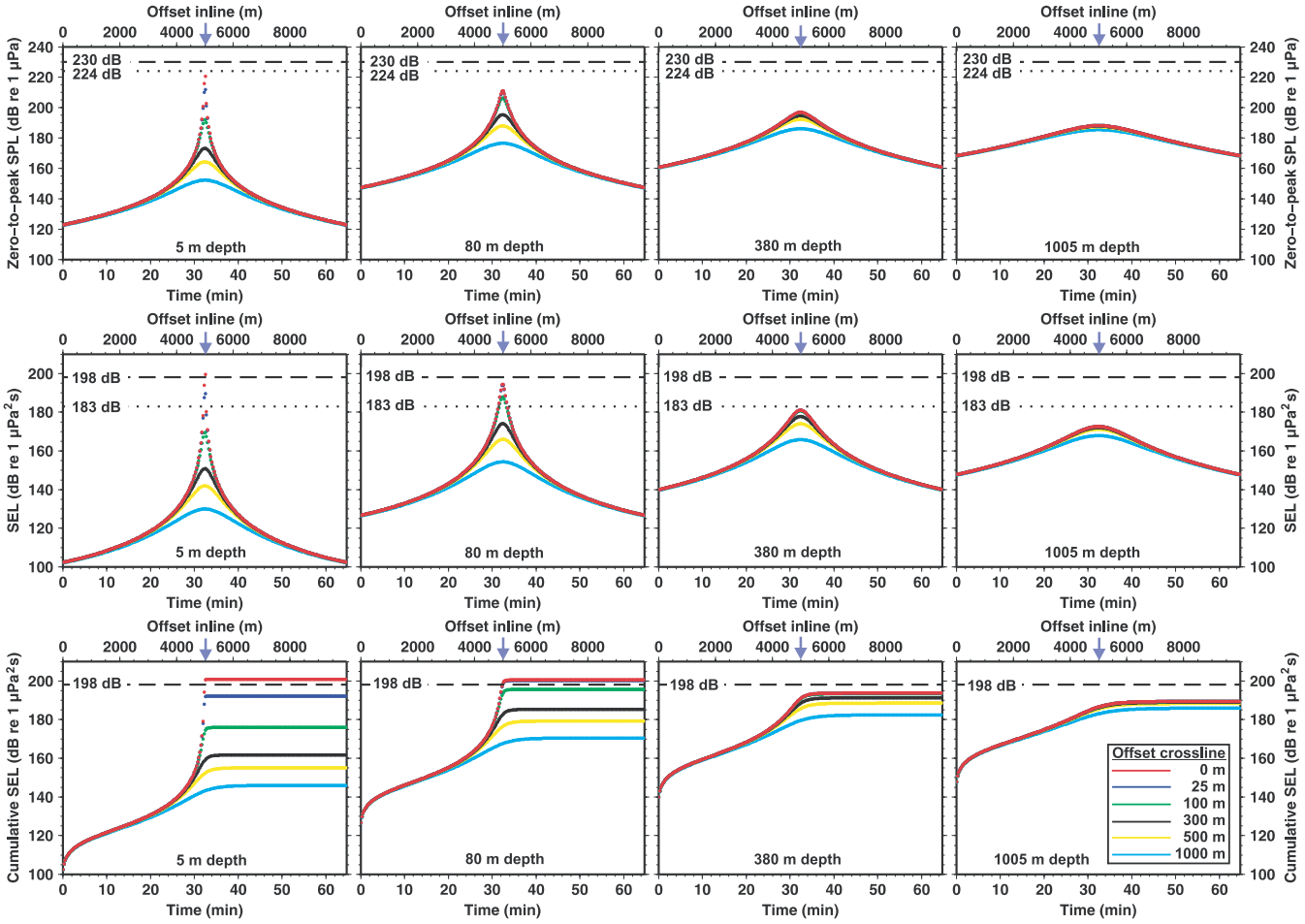

Figure 8. Semi-infinite *iso*-velocity model. 0-p SPLs and SELs of single shots (rows 1, 2) and exposure histories of multiples shots (row 3) of the 8 G-gun cluster received by marine mammals staying at 5000 m offset inline (blue arrows), various positions crossline (see legend for colours) and in 5, 80, 380 and 1005 m depth. The lower and upper abscissae indicate the survey time and source position inline. The thresholds for PTS and TTS in cetaceans due to single and multiple shots (Southall *et al.* 2007) are marked by dashed and dotted lines.

that the seismically induced noise levels received from far offsets (= 0 m offset inline here) are ∼30–50 dB higher in greater depths than close to the sea surface.

4.2 Deep and shallow water *iso*-velocity models

The deep and shallow water *iso*-velocity models demonstrate the influence of the seafloor reflections and the water depth on the SPLs and SELs. Additionally, synthetic seismogram sections illustrate the sequences of pulses marine mammals receive in different diving depths.

4.2.1 Deep water iso-velocity model

In the seismogram section in 5 m depth the amplitudes of the primary pulse decrease rapidly due to the Lloyd mirror effect, so that they are lower than the seafloor and the multiple reflections for offsets greater than ∼4 km (Fig. 9). In 80 m depth the primary pulse, the seafloor and the first multiple reflection appear with strong amplitudes over the entire 10 km range, whereas the second multiple reflection is quite weak. In 1205 m depth reflections from the sea surface and seafloor are well separated in time and appear as strong single arrivals at almost equidistant intervals. In 2605 m depth the seismogram section is similar, but the time regime of the arrivals has changed.

The SEL field of shot 1 still shows the dipole-like directivity, but compared to the semi-infinite model the levels close to the sea surface are higher for inline offsets greater than ∼1.5 km (Fig. 9). Here, the seafloor and the multiple reflections contribute considerably to the SELs and compensate the low, evanescent primary pulse.

The cumulative SEL field of 241 shots differs from the semi-infinite model mainly crossline and in the horizontal section (Fig. 9). Crossline, levels close to the sea surface are higher due to the higher levels of the single shots. This results in almost constant levels of 166–168 dB for crossline offsets greater than ∼1.5 km in the horizontal section. Closer to the seismic line levels increase rapidly and exceed the 180 dB contour line at almost the same offsets as in the semi-infinite model.

The 0-p SPLs and SELs received from single shots differ from those in the semi-infinite model mainly in shallow depths (≤80 m), such that the seismically induced noise at far offsets is higher, and the offsets inline, from which an animal receives rapidly increasing or decreasing levels, are confined to narrow ranges (Fig. 10). In 5 m depth the seismically induced noise is ∼30 dB (0-p) and ∼35 dB (SEL) higher than in the semi-infinite model, and SPLs and SELs, which exceed these noise levels, confine to ∼4.5–5.5 km

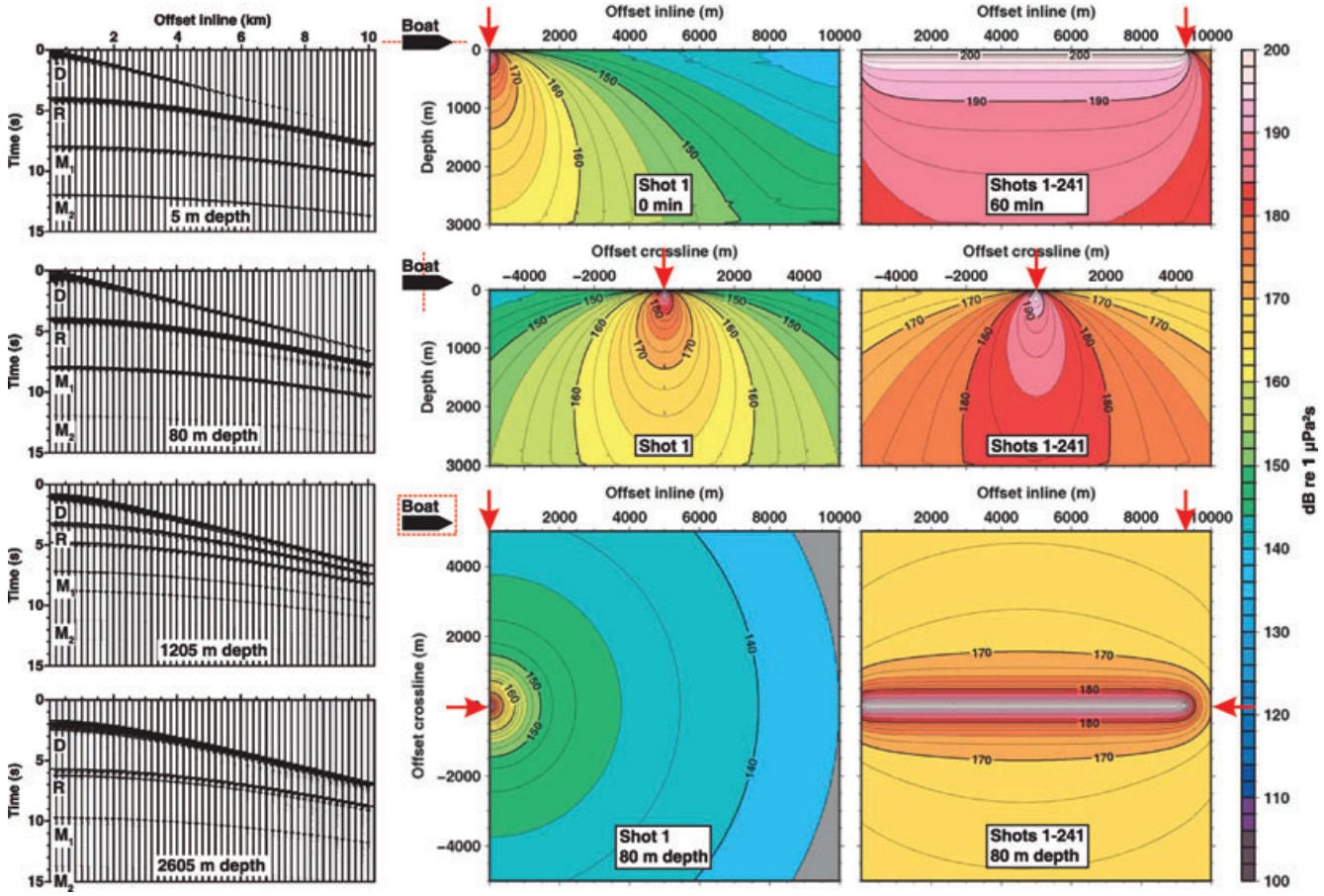

Figure 9. Deep water *iso*-velocity model. Synthetic seismogram sections in 5, 80, 1205 and 2605 m depth (column 1) and SEL fields of a single shot (column 2) and 241 superposed shots (column 3) emitted by the 8 G-gun cluster. Rows 1, 2 display the inline- and crossline-depth sections, row 3 the horizontal section in 80 m depth. The red arrows mark the position of the ship after 0 and 60 min survey time at 0 and 9260 m offset inline. D = primary pulse, R = seafloor reflection, M_1, M_2 = 1st and second multiple reflection.

offset inline. With greater depths these inline offset ranges become broader, and the curves resemble those in the semi-infinite model. Only the seismically induced noise at far offsets is slightly higher.

Accordingly, the exposure histories also start with higher noise levels as in the semi-infinite model, but the thresholds for PTS and TTS are exceeded at the same depth/crossline positions (Fig. 10). In addition, the exposure histories close to the sea surface are almost independent of the crossline position, if the animal is more than 300 m away from the seismic line due to the acoustic impact of the seafloor and the multiple reflections.

4.2.2 Shallow water iso-velocity model

The synthetic seismogram sections displayed for 5, 80, 205 and 355 m depth reveal strong wave trains, in which the arrivals of the primary pulse and the seafloor and multiple reflections can only hardly be identified (Fig. 11). Hence, in shallow waters marine mammals hear a long continuous wave train rather than a series of short pulses.

In the SEL field of shot 1 the dipole-like directivity is not clearly obvious any more, partly due the vertical exaggeration. Levels are generally ∼10–12 dB higher than in the deep water model, decrease more slowly with range and are almost independent of depth along the entire offset range (Fig. 11). In the horizontal section slight undulations between 154 and 156 dB occur with increasing offset.

The cumulative SELs of 241 shots differ only slightly from those in the deep-water model inline (Fig. 11). Crossline, they are again ∼10–12 dB higher, so that the 180 dB contour line in the horizontal section extends to significantly larger offsets crossline than in the deep water model. However levels higher than 190 dB still confine to a narrow area close to the seismic line.

The 0-p SPLs and SELs received from single shots mainly differ from the deep-water curves in the seismically induced noise at far offsets (Fig. 12). As described above, levels are on average ∼10 dB higher and show slight undulations of ∼5–10 dB. Accordingly, exposure histories also start with ∼10 dB higher noise levels. In addition, exposure histories received close to the sea surface are already nearly independent of the offset crossline, if animals are more than 100 m away from the seismic line, in contrast to ∼300 m offset and ∼5–10 dB lower plateau levels in deep waters. However the thresholds for PTS and TTS are again exceeded at the same depth/offset crossline pairs as in the deep water and semi-infinite *iso*-velocity model.

4.3 Amundsen/Bellingshausen Sea and Weddell Sea models

The modelling computations for the Amundsen/Bellingshausen and Weddell Sea illustrate the refractive effect of the sound velocity

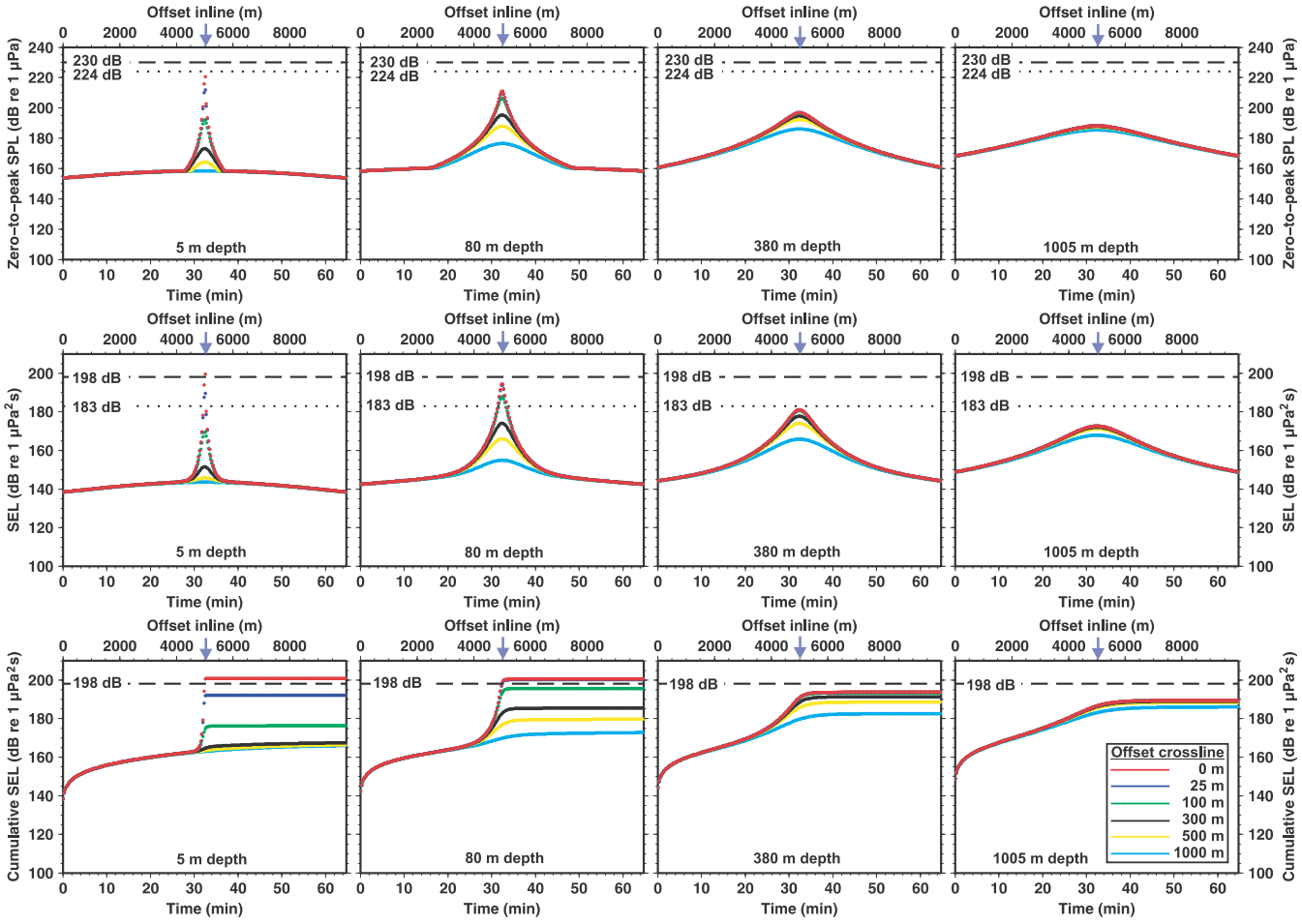

Figure 10. Deep water *iso*-velocity model. 0-p SPLs and SELs of single shots (rows 1, 2) and exposure histories of multiples shots (row 3) of the 8 G-gun cluster received by marine mammals staying at 5000 m offset inline (blue arrows), various positions crossline (see legend for colours) and in 5, 80, 380 and 1005 m depth. The lower and upper abscissae indicate the survey time and source position inline. The thresholds for PTS and TTS in cetaceans due to single and multiple shots (Southall *et al.* 2007) are marked by dashed and dotted lines.

profiles of the water column. Of particular interest is the influence of the near-surface low-velocity channels and the underlying sound velocity gradients. Additionally, the influence of the shot interval and the physical properties of the seafloor are investigated, and the acoustic impacts of all air-gun configurations are compared.

4.3.1 Deep-water models: Hydrographic stations 715 (Amundsen/Bellingshausen Sea) and 25 (Weddell Sea)

In both models, the SEL fields of shot 1 show a distortion of the contour lines inline and crossline ∼1000 m below the sea surface (Fig. 13). This mainly results from the sound velocity gradients beneath the low-velocity channels. The channels themselves also cause some distortion, but their effect on higher SELs is less pronounced than the effect of the underlying gradients. SELs trapped in the channel are quite low due to the source position above the channel and do not exceed 150–152 dB, as is illustrated by the zoom to the upper 400 m (Fig. 14). Slightly enhanced levels also occur below 2000 m depth for offsets greater than ∼8 km due to wide angle reflections beyond the half critical distance of 8082 m (Fig. 13, Table 3). In the horizontal section located in the channel axis SELs decrease more slowly than in the corresponding section of the deep-water *iso*-velocity model leading to ∼2–4 dB higher levels beyond ∼1 km offset.

The cumulative SELs of 241 shots nearly agree with those of the deep-water *iso*-velocity model inline. This means, that the influence of the sound velocity profile is almost negligible vertically beneath the seismic line (Figs 13 and 14). Crossline, the bulges in the contour lines caused by the sound velocity gradients and the low-velocity channels are still obvious, but similar to the single shot cumulative SELs trapped in the waveguides are rather low and do not exceed 170–172 dB. As well, cumulative SELs decrease more slowly along the channel axis in 80 m depth than in the same depth in the *iso*-velocity model, which leads to ∼4–6 dB higher seismically induced noise levels in the horizontal sections (Fig. 13). Generally, these noise levels are ∼2 dB higher in the Weddell Sea sound channel than in the Amundsen/Bellingshausen Sea sound channel. Otherwise, contour lines with levels higher than 180 dB enclose nearly the same narrow area along the seismic line as in the *iso*-velocity model.

The single shot 0-p SPLs and SELs and the exposure histories do not differ significantly from the deep-water *iso*-velocity model, particularly in greater depth (≥380 m). Only the exposure histories received in the channel axis in 80 m depth start with ∼5 dB higher cumulative SELs (Fig. 15). In addition, the levels received

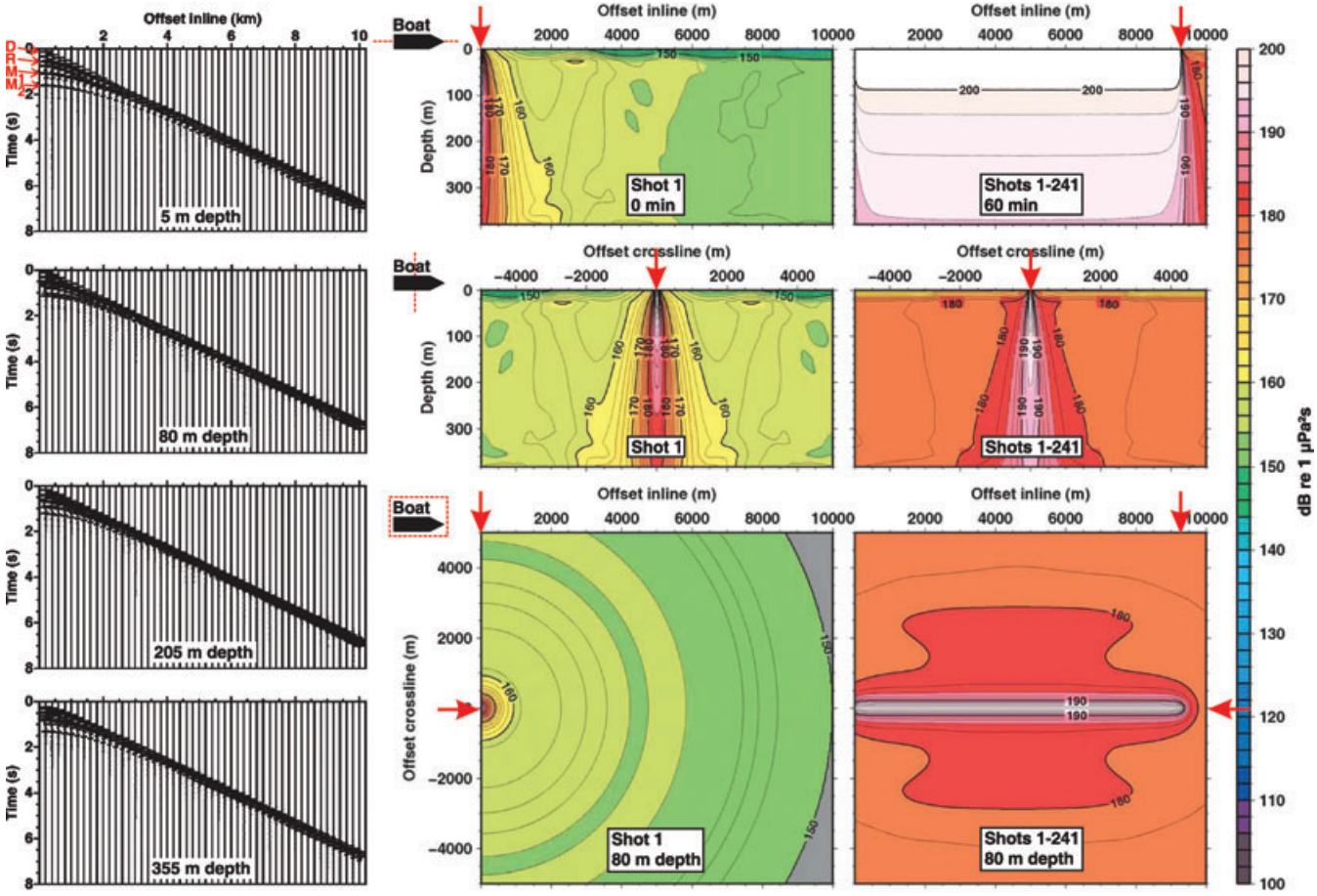

Figure 11. Shallow water *iso*-velocity model. Synthetic seismogram sections in 5, 80, 205 and 355 m depth (column 1) and SEL fields of a single shot (column 2) and 241 superposed shots (column 3) emitted by the 8 G-gun cluster. Rows 1, 2 display the inline- and crossline-depth sections, row 3 the horizontal section in 80 m depth. The red arrows mark the position of the ship after 0 and 60 min survey time at 0 and 9260 m offset inline. D = primary pulse, R = seafloor reflection, M_1, M_2 = 1st and 2nd multiple reflection.

from single shots reveal slight undulations at far offsets. However the thresholds for TTS and PTS are again exceeded at the same depth/offset crossline pairs as in the *iso*-velocity models with and without seafloor.

4.3.2 Shallow water models: Hydrographic stations 687 (Amundsen/Bellingshausen Sea) and 7 (Weddell Sea)

In both models, neither refraction due to the sound velocity profiles nor sound channelling in the low-velocity layers nor contributions from wide-angle reflections beyond the half critical distance of 1078 m are discernible (Fig. 16, Table 3). Rather the acoustic impact of both single shots and 241 superposed shots are enhanced crossline by ∼10–12 dB compared to the deep-water Southern Ocean models, and by ∼2–4 dB compared to the shallow water *iso*-velocity model. This is in good agreement with the ∼10–12 dB SEL difference between the deep and the shallow water *iso*-velocity model (*cf*. Section 4.2.2) and the ∼4–6 dB SEL difference between the deep water Southern Ocean and the deep water *iso*-velocity model in the depth of the sound channel axis (*cf*. Section 4.3.1). In other words, a ∼10 dB SEL increase can generally be attributed to the shallower water depth and a ∼5 dB SEL increase to the sound velocity profile. In the horizontal sections in 80 m depth almost the whole areas are ensonified by cumulative SELs of ∼180–184 dB, so that among all considered configurations these models cause the highest acoustic impacts. As well, cumulative SELs are ∼2 dB higher in the Weddell Sea model than in the Amundsen/Bellingshausen Sea model (*cf*. Section 4.3.1).

The single shot 0-p SPLs and SELs and the exposure histories also confirm these findings (Fig. 17). At far offsets the seismically induced noise levels of single shots are on average ∼10 dB higher than in the deep-water Southern Ocean models. Exposure histories received after 1 hour survey time are almost independent of the offset crossline, if the animal stays in 5 m depth and more than 100 m away from the seismic line, or in 80 m depth and more than 300 m away. As well, exposure histories in 80 m depth start with ∼5 dB higher levels as in the *iso*-velocity model. In greater depth the curves do not differ significantly from the shallow water *iso*-velocity model. Thresholds for TTS and PTS are again exceeded at the same depth/offset crossline pairs as in the shallow water *iso*-velocity and deep-water Southern Ocean models.

4.3.3 Variation of the shot interval

The influence of the shot interval of the 8 G-gun cluster on the maximum exposure histories received after 1 hour survey time is studied in both Weddell Sea models as example. Intervals of 15, 30 and 60 s are chosen, so that 241, 121 and 61 shots are superposed.

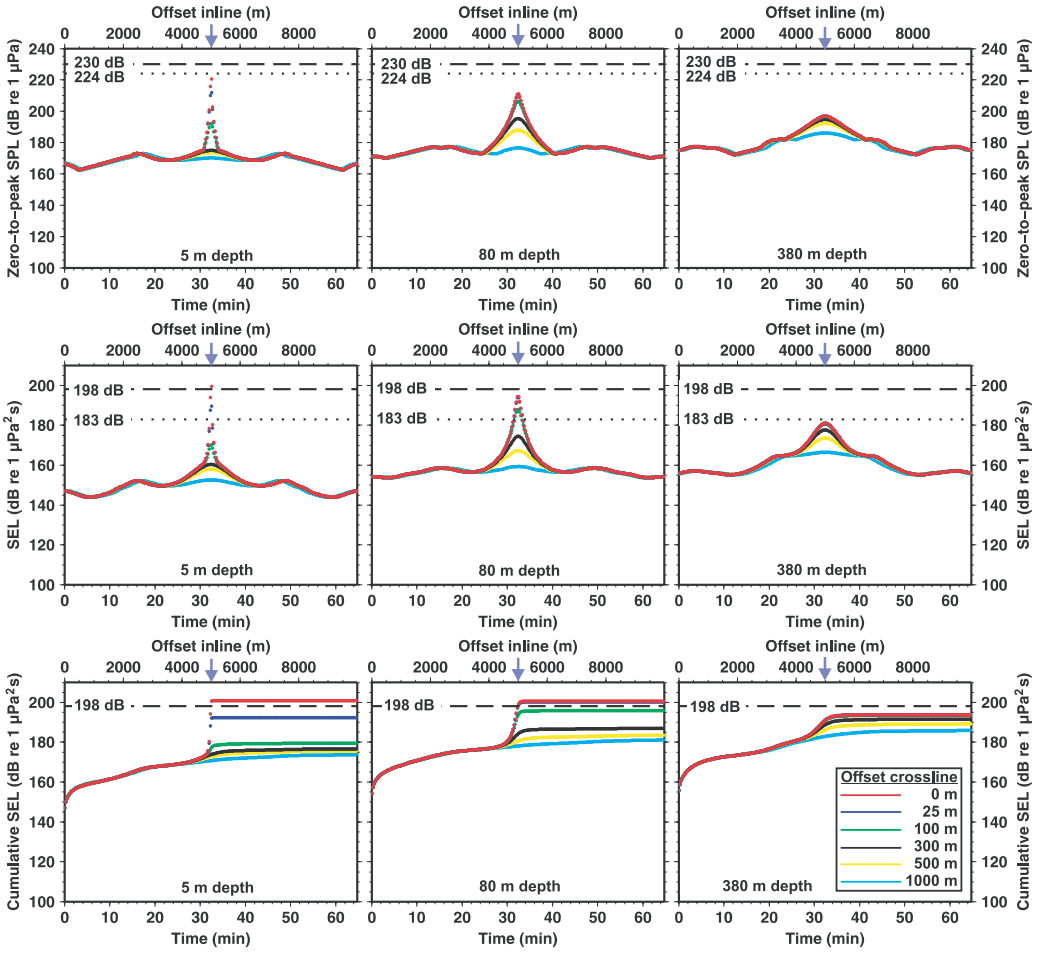

Figure 12. Shallow water *iso*-velocity model. 0-p SPLs and SELs of single shots (rows 1, 2) and exposure histories of multiples shots (row 3) of the 8 G-gun cluster received by marine mammals staying at 5000 m offset inline (blue arrows), various positions crossline (see legend for colours) and in 5, 80, 380 m depth. The lower and upper abscissae indicate the survey time and source position inline. The thresholds for PTS and TTS in cetaceans due to single and multiple shots (Southall *et al.* 2007) are marked by dashed and dotted lines.

The cumulative SEL fields of both models reveal, that levels are reduced by ∼3 dB, if the shot interval is halved (Fig. 18). Levels higher than the 198 dB threshold for PTS are confined to depths and offsets crossline less than ∼100 m for a shot interval of 15 s. For longer shot intervals the 198 dB contour line cannot be distinguished anymore, i.e. the PTS exposure zone along the seismic line is smaller than ∼100 m. Sound channelling in the near-surface duct of the deep water model is obvious for all three shot intervals, but levels also decrease by ∼3 dB per halving the shot interval (Figs 18a and b).

4.3.4 Variation of the physical properties of the seafloor

How different physical properties of the seafloor affect the maximum exposure histories received after 1 hr survey time is investigated by varying the normal incidence reflection coefficient R between 0.1 and 0.4 in both Weddell Sea models as example (Table 3).

The cumulative SEL fields of the deep-water model reveal, that moderate levels less than ∼170 dB successively increase beyond ∼5–6 km offset crossline for $R = 0.1$, 0.2 and 0.3 due to the stronger seafloor reflections and reverberations (Fig. 19a). This also applies for the cumulative SELs in the near-surface duct (Fig. 19b). The distortion of the contour lines close to the seafloor due to wide-angle reflections only appears for $R = 0.2$ and 0.3. Here, the half critical distance ranges between ∼6 and 8 km, but lies outside the model for $R = 0.1$ (Table 3). If the seafloor is very hard ($R = 0.4$), the contributions of the seafloor and multiple reflections dominate over the refractive properties of the water column (Figs 19a and b). Neither sound channelling in the near-surface duct nor distortions of the contour lines due to the sound velocity gradient and wide angle reflections are discernible any more, but overlap and lead to somewhat distorted contour lines of 174–180 dB.

In the shallow water models the acoustic impact also rises with harder seafloor, but the general characteristic—almost constant levels over the whole depth range—is maintained (Fig. 19c). The most prominent increase occurs, if the reflection coefficient jumps from 0.1 to 0.2.

Critical levels such as the 198 dB threshold for PTS in cetaceans are not affected by the properties of the seafloor. Only moderate levels like the 186 dB threshold for PTS in pinnipeds slightly increase their extent, particularly in shallow waters if $R \geq 0.2$.

4.3.5 Maximum exposure histories of all air-gun configurations

The maximum exposure histories received after 1 hr firing with the four different air-gun configurations are compared for both

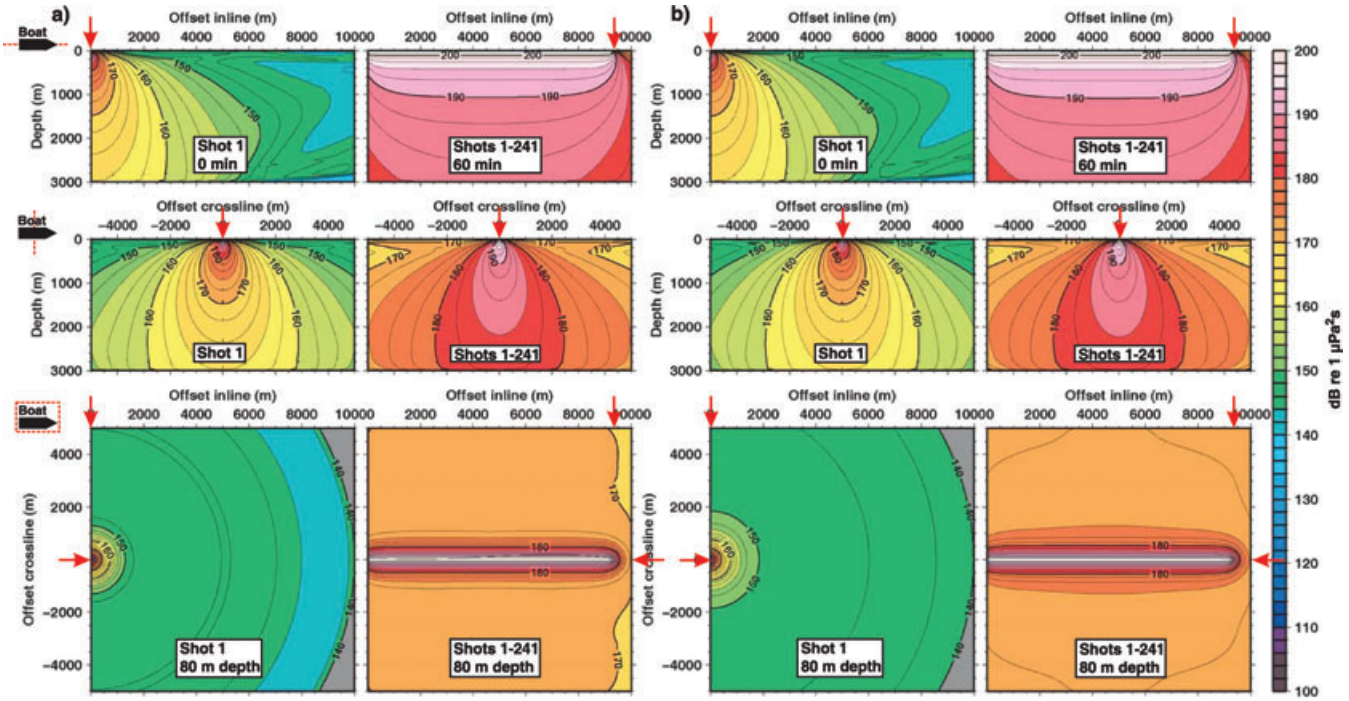

Figure 13. Deep water models for the Amundsen/Bellingshausen Sea (a) and the Weddell Sea (b). SEL inline- and crossline-depth sections (rows 1, 2) and horizontal section 80 m below the sea surface (row 3) generated by a single shot (columns 1, 3) and the superposition of 241 shots (columns 2, 4) of the 8 G-gun cluster. The red arrows mark the position of the ship after 0 and 60 min survey time at 0 and 9260 m offset inline.

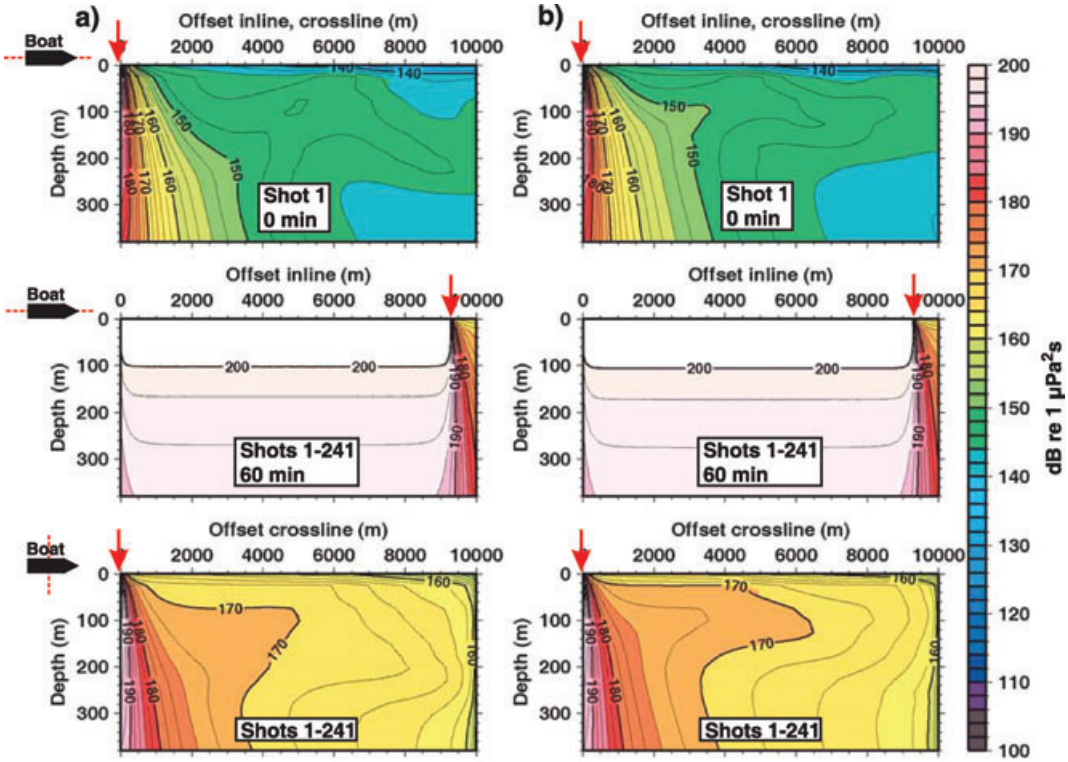

Figure 14. Deep water models for the Amundsen/Bellingshausen Sea (a) and the Weddell Sea (b). Zoom to the upper 400 m of the water column. Row 1 displays the SEL inline-depth sections of a single shot, rows 2, 3 the cumulative SEL inline- and crossline-depth sections of 241 superposed shots emitted by the 8 G-gun cluster. The red arrows mark the position of the ship after 0 and 60 min survey time at 0 and 9260 m offset inline.

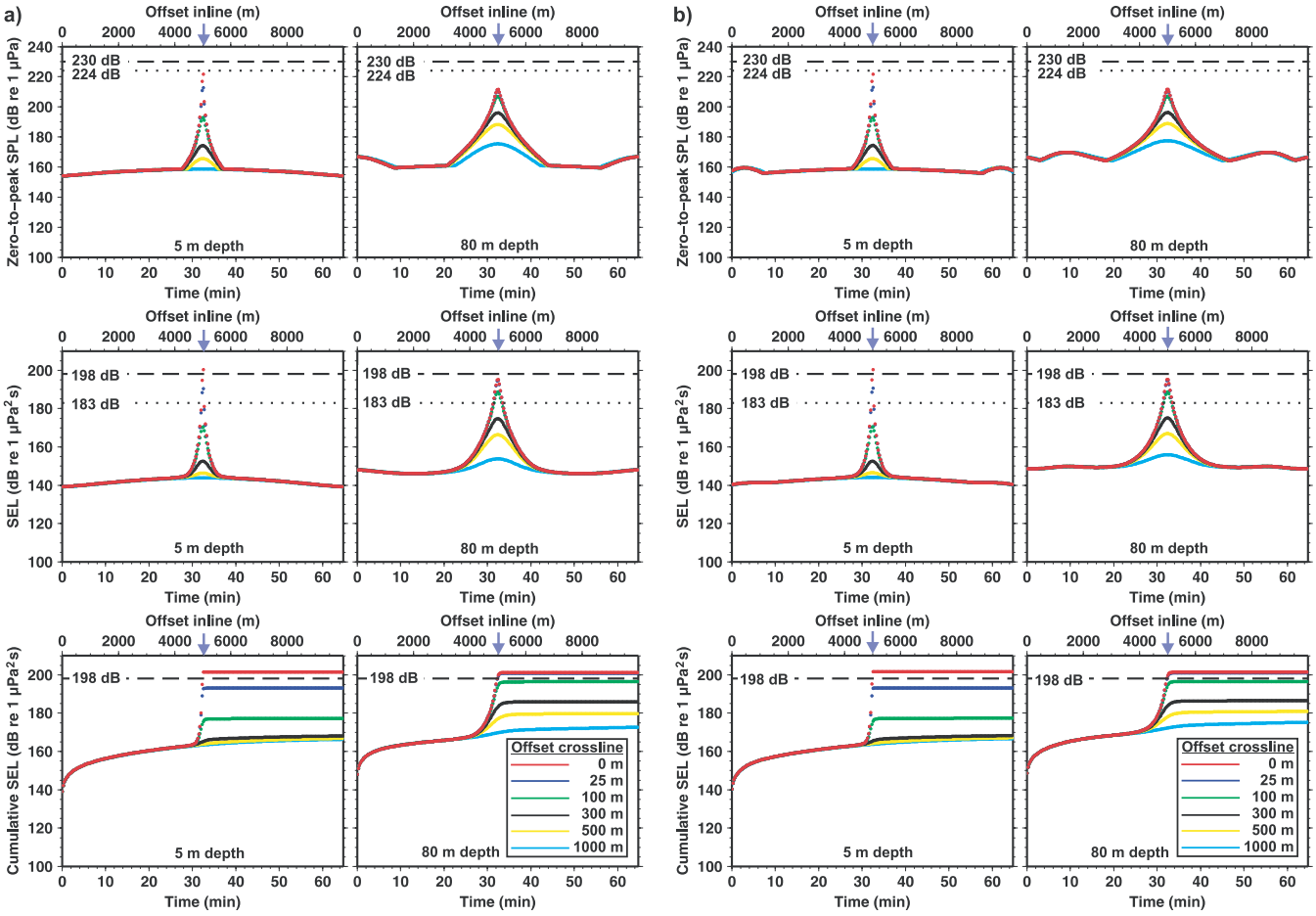

Figure 15. Deep water models for the Amundsen/Bellingshausen Sea (a) and the Weddell Sea (b). 0-p SPLs and SELs of single shots (rows 1, 2) and exposure histories of multiples shots (row 3) of the 8 G-gun cluster received by marine mammals staying at 5000 m offset inline (blue arrows), various positions crossline (see legend for colours) and in 5 and 80 m depth. The lower and upper abscissae indicate the survey time and source position inline. The thresholds for PTS and TTS in cetaceans due to single and multiple shots (Southall *et al.* 2007) are marked by dashed and dotted lines. In 380 and 1005 m depth the curves almost agree with those of the deep water *iso*-velocity model (Fig. 10) and are therefore not displayed here.

Weddell Sea models as example (Fig. 20). The 8 G-gun cluster fired at intervals of 15 s generates the highest acoustic impact. It is followed by the 8 G + 1 Bolt-gun cluster, which produces ∼3–4 dB lower cumulative SELs due to its longer shot interval, though its SL_{SE} is 3 dB higher (Table 5). The 1 G gun and the 3 GI-gun cluster cause comparatively low and similar acoustic impacts. Their cumulative SELs are ∼12–16 dB lower than those of both 8 G-gun cluster configurations.

4.3.6 Rms SPLs

The rms SPL fields are similar to the 0-p SPL and SELs of single shots and are therefore not displayed here. However, they are included in the subsequent discussion of exposure zone radii, which takes the rms level and the dual noise exposure criterion into account.

5 DISCUSSION

5.1 Exposure zone radii

From the 0-p and rms SPLs and SELs of the single shots and the maximum exposure histories of all air-gun shots exposure zone radii are derived, within which the thresholds for PTS and TTS according to the dual criterion and for Level A and B harassment according to the rms-level criterion (*cf*. Section 1) are exceeded (Tables 6–9). These radii are defined as the total distance between source and receiver and are computed from the maximum offset crossline h_{max}, where the threshold is exceeded, and the corresponding receiver depth z according to $r = (h_{max}^2 + z^2)^{1/2}$. In contrast to the definition of Southall *et al.* (2007) no M-weighting is applied to the SEL computations before radii are derived. That means though the radii discussed below refer to the specific thresholds for cetaceans and pinnipeds, the hearing sensitivities of low-, mid- and high-frequency cetaceans and pinnipeds are neglected. As these hearing sensitivities imply a bandpass filtering of the received acoustic signals, which can reduce the signal strength, the radii discussed below are again upper limits, in addition to the potential overestimation of the radii due to the point source approximation (*cf*. Sections 3.1 and 5.2). Further information on the hearing sensitivities of low-, mid-, and high-frequency cetaceans and pinnipeds and the M-weighting filter characteristics are given in the Appendix.

For fixed air-gun configurations the radii do not vary strongly between the different models, indicating that neither the sound velocity profile nor the water depth nor the physical properties of the seafloor play an important role. In detail, exposure zones, within which marine mammals according to the dual criterion might

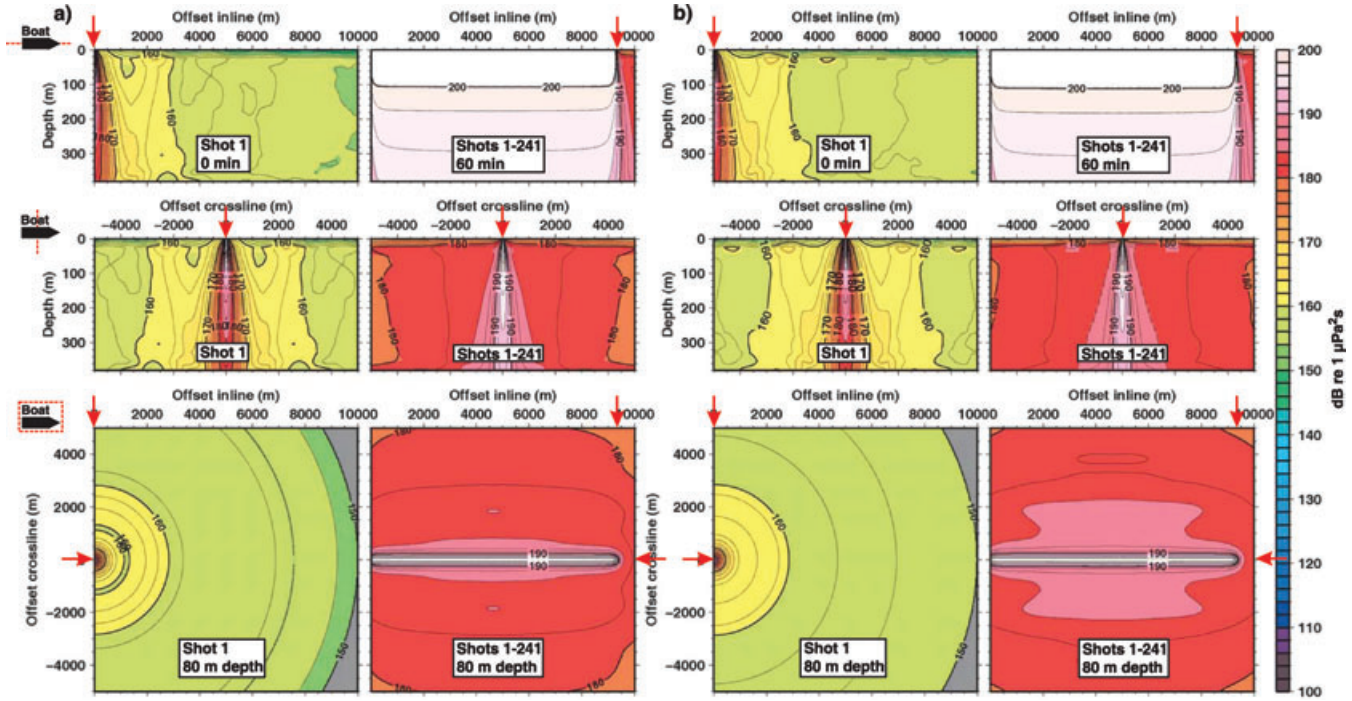

Figure 16. Shallow water models for the Amundsen/Bellingshausen Sea (a) and the Weddell Sea (b). SEL inline- and crossline-depth sections (rows 1, 2) and horizontal section 80 m below the sea surface (row 3) generated by a single shot (columns 1, 3) and the superposition of 241 shots (columns 2, 4) of the 8 G-gun cluster. The red arrows mark the position of the ship after 0 and 60 min survey time at 0 and 9260 m offset inline.

experience a PTS due to the SELs of a single shot, have radii between 25 and 58 m for cetaceans and 25 and 239 m for pinnipeds and reach depths of maximum 30 and 130 m, respectively (Table 6). If the thresholds for TTS are considered, radii increase to 25–329 m for cetaceans and 104–1499 m for pinnipeds with maximum depths of 180 and 780 m, respectively (Table 7).

The radii of the 0-p thresholds are significantly smaller and amount to 25–58 m for PTS and 25–104 m for TTS in cetaceans and pinnipeds (Tables 6, 7). The variation range of the radii in the different models increases with lower thresholds and for airgun clusters with large volumes. The physical properties of the seafloor affect only the 171 dB SEL radii in the shallow water models, such that the radii increase slightly for reflection coefficients $R \geq 0.2$.

The exposure zone radii, within which marine mammals might experience a PTS due to multiple shots, approximately doubled for cetaceans and increased on average tenfold for pinnipeds compared to the single shot radii (Table 8). This means, cumulative SEL radii reach 25–128 m extent and maximum 80 m depth for cetaceans and 25–3700 m extent and maximum 1380 m depth for pinnipeds. An increasing reflection coefficient of the seafloor again leads to only slightly larger radii in shallow waters. A doubling of the shot interval of the 8 G-gun cluster approximately results in halving the radii. Accordingly, the radii required to mitigate the 8 G-gun cluster are larger than the radii required for the 8 G + 1 Bolt-gun cluster due to the shorter shot interval (*cf*. Sections 4.3.3 and 4.3.5).

The radii, where the rms SPLs of single shots fall below the 180 dB threshold for Level A harassment in cetaceans, range between the 183 and 171 dB SEL radii for single shots, whereas the 190 dB rms radii for Level A harassment in pinnipeds almost agree with the 183 dB SEL radii (Table 9). Hence, though the SELs are derived from the total seismogram duration and the rms SPLs from a window of 200 ms length (*cf*. Section 3.2), the rms window length T (in s) can be used to approximately convert rms SPLs (SPL_{rms}) to SELs according to $SEL \approx SPL_{rms} + 10 \log_{10}(T)$ (Madsen 2005). This is due to the fact, that SELs do not change significantly with increasing window length, if the dominant contributions come from a strong primary pulse and seafloor reflections within the first several hundred milliseconds of the window (Breitzke *et al.* 2008). Hence, the 160–190 dB rms radii approximately agree with ∼7 dB lower 153–183 dB SEL radii.

To study how much radii change, if thresholds will be modified due to an improved knowledge of the hearing abilities of marine mammals, radii are also determined for higher, lower and intermediate thresholds using the Weddell Sea models as example (Figs 21 and 22). Radii r start with a minimum value of 25 m and increase linearly on a logarithmic scale for a wide range of thresholds. Logarithmic least square fits to these data indicate, that in case of single shots SPL and SEL thresholds T_{single} (in dB) essentially follow a spherical spreading law $T_{single} = SL - 20 \log_{10} r$. The intercepts at $\log_{10} r = 0$ agree with the corresponding SLs with an accuracy of ±3 dB (Table 5). In case of multiple shots the decay of the cumulative SEL thresholds T_{cum} (in dB) flattens to a cylindrical spreading law $T_{cum} = SL_{SE} - 10 \log_{10} r - 10 \log_{10} \Delta T$. Here, the intercepts at $\log_{10} r = 0$ are 9–20 dB lower than the SL_{SE}s, depending on the shot interval ΔT (in s) (Table 5). The estimated precision of the predicted thresholds is at least ±3 dB. The two spreading laws are largely valid for deep and for shallow water models. The only remarkable difference occurs for radii greater than 4000 m, where the rms SPLs and SELs start to decrease faster in the deep-water models. This results from the limited model size and duration of the synthetic seismograms. Both imply, that the number of multiple reflections contributing to the SELs decrease towards the right model boundary, an effect, which is more pronounced in the deep

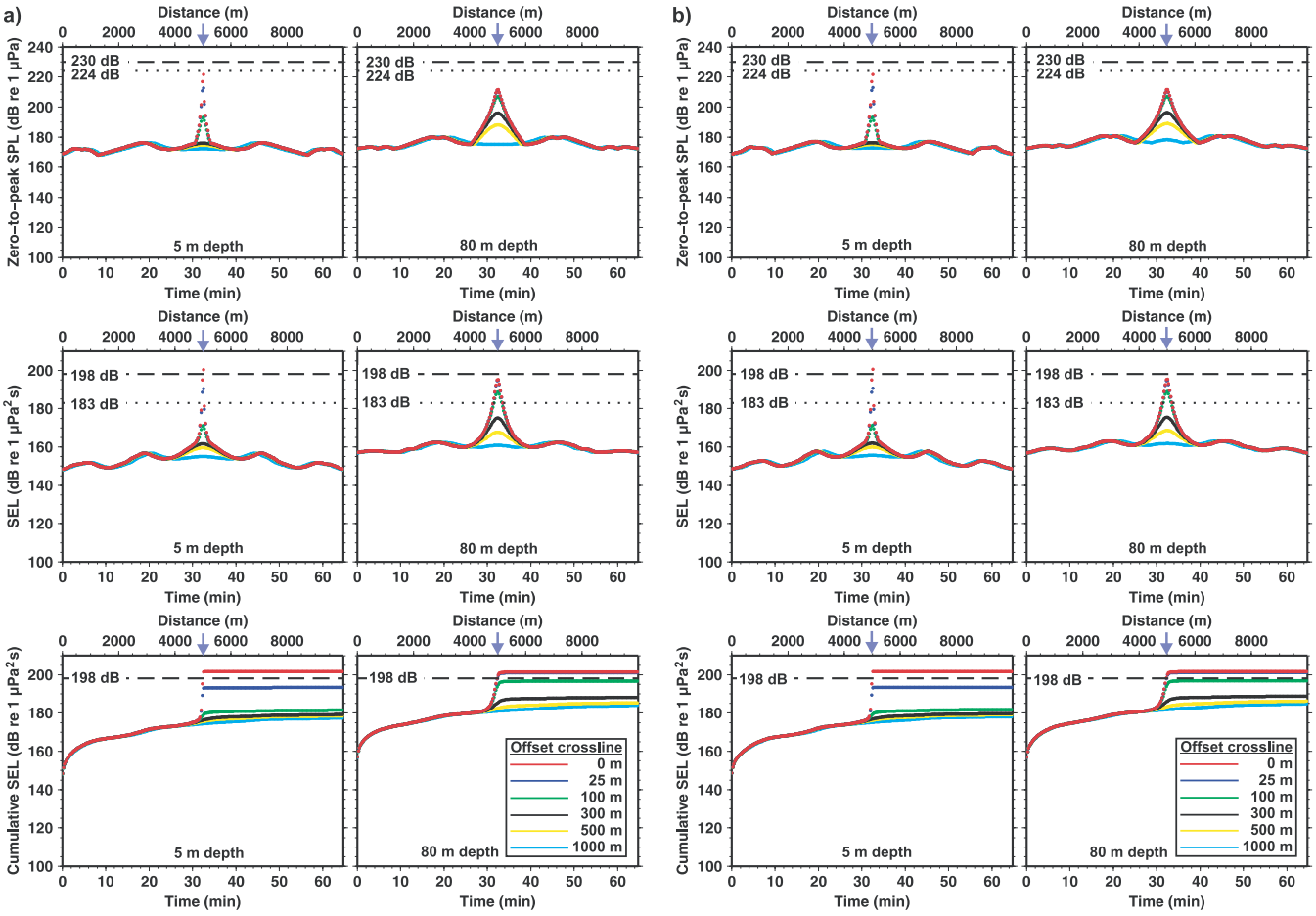

Figure 17. Shallow water models for the Amundsen/Bellingshausen Sea (a) and the Weddell Sea (b). 0-p SPLs and SELs of single shots (rows 1, 2) and exposure histories of multiples shots (row 3) of the 8 G-gun cluster received by marine mammals staying at 5000 m offset inline (blue arrows), various positions crossline (see legend for colours) and in 5 and 80 m depth. The lower and upper abscissae indicate the survey time and source position inline. The thresholds for PTS and TTS in cetaceans due to single and multiple shots (Southall *et al.* 2007) are marked by dashed and dotted lines. In 380 m depth the curves almost agree with those of the shallow water *iso*-velocity model (Fig. 12) and are therefore not displayed here.

water models, because the time lag between subsequent multiple reflections is greater than in the shallow water models.

5.2 Point source approximation and sound channelling in the near-surface ducts

Some papers suggest, that high-frequency components emitted by side lobes of wide air-gun arrays with shallow launch angles might be trapped in surface ducts, so that they appear at large ranges with levels not explainable be simple geometric spreading laws (e.g. Sidorovskaia 2004; DeRuiter *et al.* 2006; Madsen *et al.* 2006). Such conditions are discussed to be one potential trigger for stranding events, particularly if mid-frequency military sonars are used as sound sources (D'Spain *et al.* 2006). In this study, we approximated the compact air-gun clusters by point sources and limited the frequency band to maximum 256 Hz to achieve reasonable computation times. Thus, we replaced the downward focused directivities of the air-gun clusters by broader directivities of point sources and concentrated on the energy emitted by the main lobe. In the following we discuss, how sound channelling in the near-surface ducts of the Southern Ocean and exposure zone radii might change, if both approximations would be given-up.

5.2.1 *Point source approximation*

In the far-field a seismic array can be considered as a point source, because all signals emitted by the individual air guns interfere constructively. The transition to the near field, where the traveltime differences between the signals of the individual air guns cause partial destructive interferences, is defined by the Fresnel zone distance $D_F = L^2/(4\lambda)$, where L is the largest dimension of the array and λ the wavelength (Lurton 2002). If the diameter of each air-gun cluster is considered to be the largest dimension L and a maximum frequency of 256 Hz is assumed, the Fresnel zone distances amount to $\sim$5 m for the 8 G + 1 Bolt-gun cluster, $\sim$1.1 m for the 8 G-gun cluster and $\sim$0.2 m for the 3 GI-gun cluster. Thus, the grid spacing of 25 m, for which synthetic seismograms are computed, is at least five times larger than the greatest Fresnel zone distance, so that all receiver positions lie in the far-field.

However, the spacings of the individual air guns lie in the near-field and affect the directivities of the air-gun clusters. To illustrate how strong these exact directivities deviate from a point source they are modelled with the NUCLEUS^{TM} software. A comparison of the broad-band (0–1 kHz) directivities of the most silent

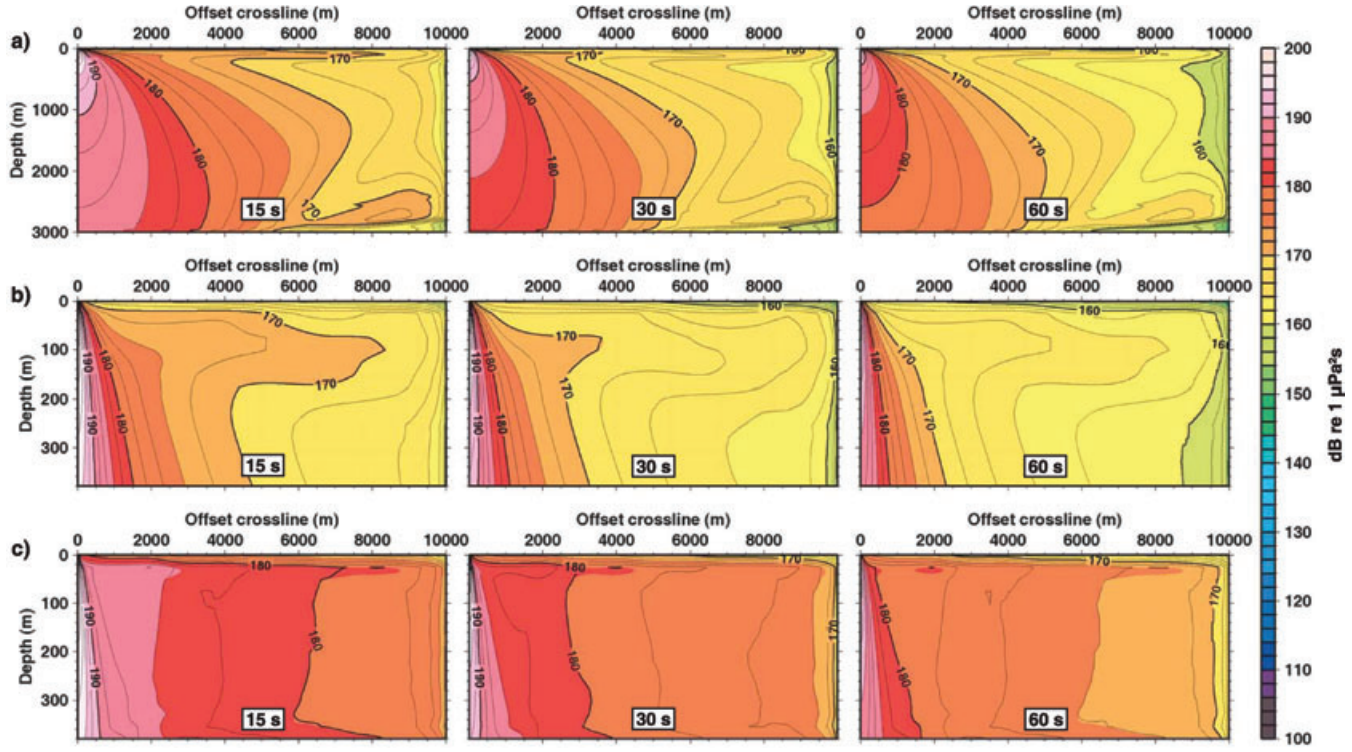

Figure 18. Deep and shallow water models for the Weddell Sea. Cumulative SELs received by marine mammals at $x = 5000$ m offset inline and any (y, z) position crossline after 1 hr firing with the 8 G-gun cluster. The shot interval is varied between 15, 30 and 60 s (columns 1–3). (a) Cumulative SELs of the deep water Weddell Sea model, (b) zoom of (a) to the upper 400 m, (c) cumulative SELs of the shallow water Weddell Sea model.

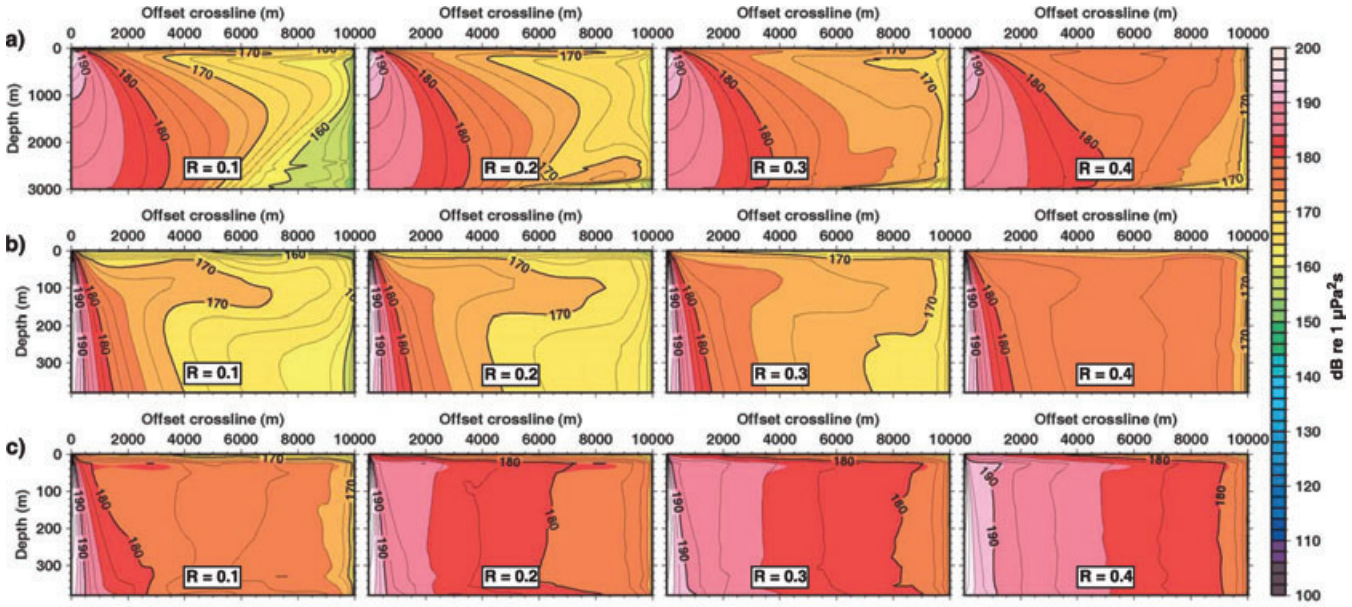

Figure 19. Deep and shallow water models for the Weddell Sea. Cumulative SELs received by marine mammals at $x = 5000$ m offset inline and any (y, z) position crossline after 1 hr firing with the 8 G-gun cluster. The normal incidence reflection coefficient R at the seafloor is varied between 0.1, 0.2, 0.3 and 0.4 (columns 1–4). (a) Cumulative SELs of the deep water Weddell Sea model, (b) zoom of (a) to the upper 400 m, (c) cumulative SELs of the shallow water Weddell Sea model.

point source—the 1 G gun—with the loudest and spatially widest source—the 8 G + 1 Bolt-gun cluster—primarily yields the downward focusing effect of the cluster geometry, particularly for frequencies above ∼300 Hz (Fig. 23). Here, side lobes occur, but their levels are at least 30 dB lower than the peak level of the main lobe, which concentrates on frequencies lower than ∼300 Hz. However even in this lower frequency range the sound radiation of the air-gun cluster is slightly more focused downwards than the sound radiation of the point source. For example, the relative amount of frequency components between ∼100 and 300 Hz

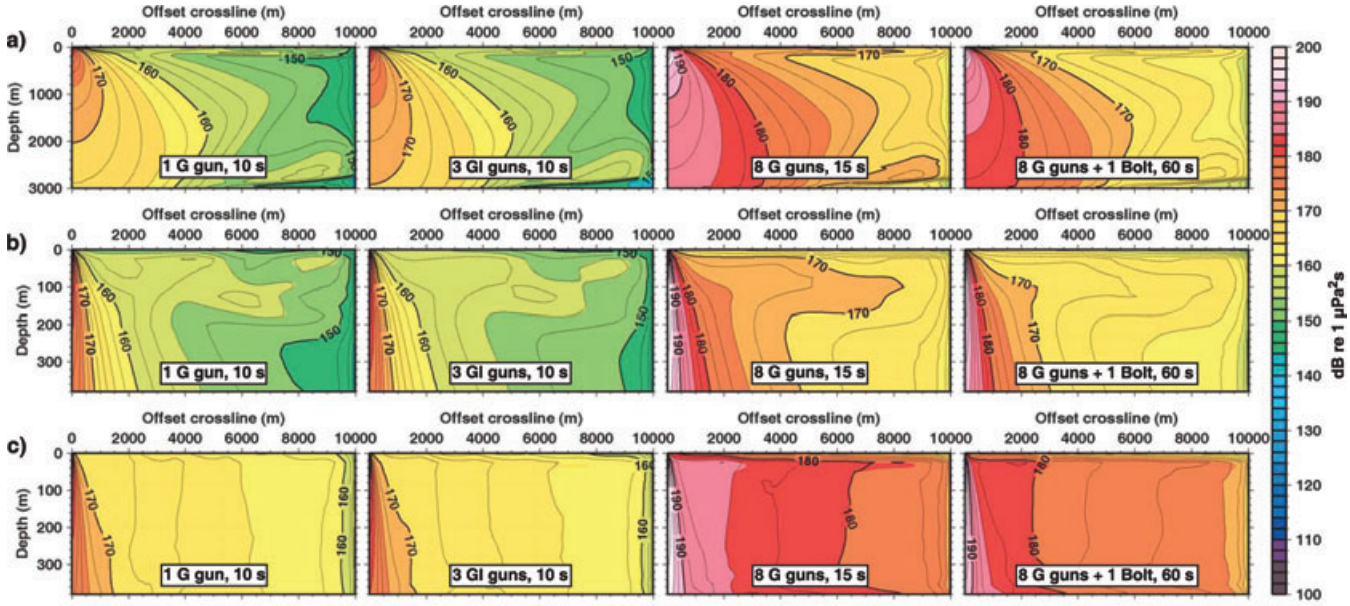

Figure 20. Deep and shallow water models for the Weddell Sea. Cumulative SELs received by marine mammals at $x = 5000$ m offset inline and any (y, z) position crossline after 1 hr firing with the four air-gun configurations at their typical shot intervals (columns 1–4). (a) Cumulative SELs of the deep water Weddell Sea model, (b) zoom of (a) to the upper 400 m, (c) cumulative SELs of the shallow water Weddell Sea model.

emitted with launch angles of 60°–90° is higher for the 1 G gun (Figs 23a and b) than for the 8 G + 1 Bolt gun cluster (Figs 23c and d). Hence, the limitation of the frequency band to maximum 256 Hz neglects a low portion of side lobe energy above 300 Hz, but the approximation of the air-gun clusters by point source equivalents simultaneously introduces some additional energy above ∼100 Hz, particularly for shallow launch angles. So, all in all we do not expect significant changes in the FD modelling results, if the point source approximation and band limitation would be given up. Rather, in the considered frequency band (0–256 Hz) the ranges and exposure zone radii derived in the previous sections can be taken as upper limits due to the increased energy between ∼100 and 300 Hz in the point source directivity compared to the cluster directivity.

5.2.2 Sound channelling in near-surface ducts

According to Jensen *et al.* (2000) the lower cut-off frequency f_0 (in Hz) of acoustic waves trapped in an *iso*-thermal surface duct of thickness D (in m) is given by $f_0 \cong 1500/(0.008D^{3/2})$. Though the sound velocity profiles used in this study are not characterized by a perfect surface limited sound duct, they are characterized by 'buried' low-velocity sound channels of different thickness, bounded above by a sharp transition to layers with higher sound velocity and below by a smooth transition to a sound velocity gradient.

If the above equation for f_0 is assumed for these sound velocity channels, the cut-off frequencies range from ∼47 to 102 Hz in the Amundsen/Bellingshausen Sea, where the thicknesses of the sound channels vary between ∼150 and 250 m, and from ∼17 to 66 Hz in the Weddell Sea with sound channel thicknesses of ∼200–500 m. Thus, in contrast to a ∼50 m thin surface duct in the Gulf of Mexico, which preferentially trapped high-frequency energy above ∼530 Hz (DeRuiter *et al.* 2006; Madsen *et al.* 2006), the sound channels in the Southern Ocean act as broadband waveguides, in which most of the low-frequency seismic energy can be channelled, too. However, with towing depths between 5 and 10 m the air-gun clusters are located above the sound channels. So, the greatest portion of the downward-directed main lobe, which leaves the source with high levels, passes the channels in almost vertical direction, whereas lower levels emitted with shallow launch angles will be refracted into and out of the channels and propagate as leaky modes (Jensen *et al.* 2000). Hence, even if the band limitation to maximum 256 Hz would be given up, and the low-level, high-frequency side lobes of the air-gun cluster directivities would be considered, they would still radiate their energy above the sound channels leading to only weak refraction into and out of the channel, so that no considerable effect on the exposure zone radii is expected.

Moreover, even if the low-velocity channel reaches up to the sea surface, as it does in the shallow water Weddell Sea model (hydrographic station 7) during the austral fall season, and the air gun clusters are located in the sound channel, we do not expect significant changes in the exposure zone radii. The reason is, that the low levels of the side lobes will still be partially refracted out of the channel at its lower gradual boundary and propagate as leaky modes. That means that the dominant portion of the seismic energy, which can be trapped in the sound channels, is already included in the band-limited models and is considered in the determination of the exposure zone radii. Moreover, as the relative amount of energy between ∼100 and 300 Hz radiated with shallow launch angles is slightly higher for the point source equivalents than for the air-gun clusters, the exposure zone radii derived in the previous sections can again be considered as upper limits.

6 CONCLUSIONS

Considering the key questions posed in Section 4 the following conclusions can be drawn.

(1) Firing multiple air-gun shots along a seismic line generates a tubular cumulative SEL field with maximum levels

Table 6. Radii, where the 0-p SPLs ($SPL_{0\text{-}p}$) and SELs of a single shot fall below the thresholds, which according to the dual criterion define the onset of PTS (injury) in cetaceans and underwater pinnipeds.

			PTS (injury), cetaceans						PTS (injury), pinnipeds					
			230 dB[a] ($SPL_{0\text{-}p}$)			198 dB[b] (SEL)			218 dB[a] ($SPL_{0\text{-}p}$)			186 dB[b] (SEL)		
Air-gun configuration/model	ΔT (s)	R	r (m)	h_{max} (m)	z (m)	r (m)	h_{max} (m)	z (m)	r (m)	h_{max} (m)	z (m)	r (m)	h_{max} (m)	z (m)
1 G-gun (8.5 l)														
Semi-infinite *iso*-velocity model	10	0.2	25	25	5	25	25	5	25	25	5	25	25	5
Deep water *iso*-velocity model	10	0.2	25	25	5	25	25	5	25	25	5	25	25	5
Amundsen/Bellingshausen Sea 715	10	0.2	25	25	5	25	25	5	25	25	5	25	25	5
Weddell Sea 25	10	0.2	25	25	5	25	25	5	25	25	5	25	25	5
Shallow water *iso*-velocity model	10	0.2	25	25	5	25	25	5	25	25	5	25	25	5
Amundsen/Bellingshausen Sea 687	10	0.2	25	25	5	25	25	5	25	25	5	25	25	5
Weddell Sea 7	10	0.2	25	25	5	25	25	5	25	25	5	25	25	5
3 GI-gun cluster (7.4 l)														
Semi-infinite *iso*-velocity model	10	0.2	25	25	5	25	25	5	25	25	5	25	25	5
Deep water *iso*-velocity model	10	0.2	25	25	5	25	25	5	25	25	5	25	25	5
Amundsen/Bellingshausen Sea 715	10	0.2	25	25	5	25	25	5	25	25	5	25	25	5
Weddell Sea 25	10	0.2	25	25	5	25	25	5	25	25	5	25	25	5
Shallow water *iso*-velocity model	10	0.2	25	25	5	25	25	5	25	25	5	25	25	5
Amundsen/Bellingshausen Sea 687	10	0.2	25	25	5	25	25	5	25	25	5	25	25	5
Weddell Sea 7	10	0.2	25	25	5	25	25	5	25	25	5	25	25	5
8 G-gun cluster (68.2 l)														
Semi-infinite *iso*-velocity model	15	0.2	25	25	5	58	50	30	58	50	30	183	150	105
Deep water *iso*-velocity model	15	0.2	25	25	5	58	50	30	58	50	30	183	150	105
Amundsen/Bellingshausen Sea 715	15	0.2	25	25	5	58	50	30	58	50	30	170	150	80
Weddell Sea 25	15	0.2	25	25	5	58	50	30	58	50	30	170	150	80
Shallow water *iso*-velocity model	15	0.2	25	25	5	58	50	30	58	50	30	183	150	105
Amundsen/Bellingshausen Sea 687	15	0.2	25	25	5	58	50	30	58	50	30	170	150	80
Weddell Sea 7	15	0.2	25	25	5	58	50	30	58	50	30	170	150	80
Weddell Sea 25	15	0.1	25	25	5	58	50	30	58	50	30	170	150	80
Weddell Sea 7	15	0.1	25	25	5	58	50	30	58	50	30	170	150	80
Weddell Sea 25	15	0.3	25	25	5	58	50	30	58	50	30	170	150	80
Weddell Sea 7	15	0.3	25	25	5	58	50	30	58	50	30	170	150	80
Weddell Sea 25	15	0.4	25	25	5	58	50	30	58	50	30	170	150	80
Weddell Sea 7	15	0.4	25	25	5	58	50	30	58	50	30	170	150	80
8 G + 1 Bolt 1500 LL-gun cluster (100.9 l)														
Semi-infinite *iso*-velocity model	60	0.2	25	25	5	58	50	30	58	50	30	192	175	80
Deep water *iso*-velocity model	60	0.2	25	25	5	58	50	30	58	50	30	192	175	80
Amundsen/Bellingshausen Sea 715	60	0.2	25	25	5	58	50	30	58	50	30	239	200	130
Weddell Sea 25	60	0.2	25	25	5	58	50	30	58	50	30	226	200	105
Shallow water *iso*-velocity model	60	0.2	25	25	5	58	50	30	58	50	30	192	175	80
Amundsen/Bellingshausen Sea 687	60	0.2	25	25	5	58	50	30	58	50	30	226	200	105
Weddell Sea 7	60	0.2	25	25	5	58	50	30	58	50	30	226	200	105

Notes: r is the total radius between source and receiver computed from the maximum horizontal offset h_{max}, where the threshold is exceeded, and the corresponding receiver depth z according to $r = (z^2 + h_{max}^2)^{1/2}$. The accuracy of h_{max} and z is equal to the spacing of the synthetic seismograms in the FD model, that is, 25 m. Values are rounded to their nearest integers. In contrast to the definition in Southall *et al.* (2007) all radii are derived from unweighted SPLs and SELs. ΔT = shot interval, R = normal incidence reflection coefficient at the seafloor.

[a]0-p SPL in dB re 1 μPa.

[b]SEL in dB re 1 μPa^2s.

vertically beneath the seismic line. Received exposure histories reach almost constant cumulative SELs after the air gun(s) passed the animal.

(2) Compared to a semi-infinite model the seafloor reflections in deep and shallow water models enhance the acoustic impact of single shots close to the sea surface and contribute to the seismically induced noise levels at far offsets.

(3) Cumulative SELs decrease more slowly in shallow waters than in deep waters due to stronger reverberations. At far offsets and close to the sea surface this leads to seismically induced noise levels of ∼140–145 dB re 1 μPa^2s in *iso*-velocity deep waters and ∼10 dB higher levels in shallow waters.

(4) Near-surface ducts and sound velocity gradients in the water column cause distortions of the SPL and SEL contour lines, particularly in deep waters. However, only low to moderate levels not relevant for critical exposure zone radii are affected. Compared to *iso*-velocity models marine mammals are stressed by ∼5 dB higher seismically induced noise levels, if they stay in the sound channel. This seismically induced noise is ∼2 dB higher in the Weddell Sea models (during the austral fall and spring season) than in the Amundsen/Bellingshausen Sea models (during the austral summer season).

(5) More consolidated ocean bottoms intensify the cumulative acoustic impact and increase the seismically induced noise.

Table 7. Radii, where the 0-p SPLs ($SPL_{0\text{-}p}$) and SELs of a single shot fall below the thresholds, which according to the dual criterion define the onset of TTS in cetaceans and underwater pinnipeds.

			TTS (behavioral disturbance), cetaceans						TTS (behavioral disturbance), pinnipeds					
			224 dB[a] ($SPL_{0\text{-}p}$)			183 dB[b] (SEL)			212 dB[a] ($SPL_{0\text{-}p}$)			171 dB[b] (SEL)		
Air-gun configuration/Model	ΔT (s)	R	r (m)	h_{max} (m)	z (m)	r (m)	h_{max} (m)	z (m)	r (m)	h_{max} (m)	z (m)	r (m)	h_{max} (m)	z (m)
1 G-gun (8.5 l)														
Semi-infinite *iso*-velocity model	10	0.2	25	25	5	25	25	5	25	25	5	114	100	55
Deep water *iso*-velocity model	10	0.2	25	25	5	25	25	5	25	25	5	114	100	55
Amundsen/Bellingshausen Sea 715	10	0.2	25	25	5	25	25	5	25	25	5	104	100	30
Weddell Sea 25	10	0.2	25	25	5	25	25	5	25	25	5	104	100	30
Shallow water *iso*-velocity model	10	0.2	25	25	5	25	25	5	25	25	5	114	100	55
Amundsen/Bellingshausen Sea 687	10	0.2	25	25	5	25	25	5	25	25	5	104	100	30
Weddell Sea 7	10	0.2	25	25	5	25	25	5	25	25	5	104	100	30
3 GI-gun cluster (7.4 l)														
Semi-infinite *iso*-velocity model	10	0.2	25	25	5	25	25	5	25	25	5	104	100	30
Deep water *iso*-velocity model	10	0.2	25	25	5	25	25	5	25	25	5	104	100	30
Amundsen/Bellingshausen Sea 715	10	0.2	25	25	5	58	50	30	25	25	5	148	125	80
Weddell Sea 25	10	0.2	25	25	5	58	50	30	25	25	5	137	125	55
Shallow water *iso*-velocity model	10	0.2	25	25	5	25	25	5	25	25	5	104	100	30
Amundsen/Bellingshausen Sea 687	10	0.2	25	25	5	58	50	30	25	25	5	148	125	80
Weddell Sea 7	10	0.2	25	25	5	58	50	30	25	25	5	137	125	55
8 G-gun cluster (68.2 l)														
Semi-infinite *iso*-velocity model	15	0.2	25	25	5	239	200	130	81	75	30	884	725	505
Deep water *iso*-velocity model	15	0.2	25	25	5	239	200	130	81	75	30	884	725	505
Amundsen/Bellingshausen Sea 715	15	0.2	25	25	5	226	200	105	81	75	30	960	800	530
Weddell Sea 25	15	0.2	25	25	5	226	200	105	81	75	30	946	800	505
Shallow water *iso*-velocity model	15	0.2	25	25	5	239	200	130	81	75	30	751	675	330
Amundsen/Bellingshausen Sea 687	15	0.2	25	25	5	226	200	105	81	75	30	819	750	330
Weddell Sea 7	15	0.2	25	25	5	273	225	155	81	75	30	852	775	355
Weddell Sea 25	15	0.1	25	25	5	226	200	105	81	75	30	946	800	505
Weddell Sea 7	15	0.1	25	25	5	226	200	105	81	75	30	830	750	355
Weddell Sea 25	15	0.3	25	25	5	226	200	105	81	75	30	946	800	505
Weddell Sea 7	15	0.3	25	25	5	273	225	155	81	75	30	1259	1200	380
Weddell Sea 25	15	0.4	25	25	5	226	200	105	81	75	30	1038	825	630
Weddell Sea 7	15	0.4	25	25	5	260	225	130	81	75	30	1211	1150	380
8 G + 1 Bolt 1500 LL-gun cluster (100.9 l)														
Semi-infinite *iso*-velocity model	60	0.2	25	25	5	294	250	155	81	75	30	1154	950	655
Deep water *iso*-velocity model	60	0.2	25	25	5	294	250	155	81	75	30	1154	950	655
Amundsen/Bellingshausen Sea 715	60	0.2	25	25	5	329	275	180	104	100	30	1265	1050	705
Weddell Sea 25	60	0.2	25	25	5	316	275	155	104	100	30	1328	1075	780
Shallow water *iso*-velocity model	60	0.2	25	25	5	294	250	155	81	75	30	889	825	330
Amundsen/Bellingshausen Sea 687	60	0.2	25	25	5	316	275	155	104	100	30	1451	1400	380
Weddell Sea 7	60	0.2	25	25	5	316	275	155	104	100	30	1499	1450	380

Notes: r is the total radius between source and receiver computed from the maximum horizontal offset h_{max}, where the threshold is exceeded, and the corresponding receiver depth z according to $r = (z^2 + h_{max}^2)^{1/2}$. The accuracy of h_{max} and z is equal to the spacing of the synthetic seismograms in the FD model, that is, 25 m. Values are rounded to their nearest integers. In contrast to the definition in Southall *et al.* (2007) all radii are derived from unweighted SPLs and SELs. ΔT = shot interval, R = normal incidence reflection coefficient at the seafloor.
[a]0-p SPL in dB re 1 μPa.
[b]SEL in dB re 1 μPa^{2}s.

However critical exposure zone radii are only affected in shallow waters, if moderate thresholds are considered and $R \geq 0.2$.

(6) Exposure histories received close to the sea surface depend strongly on the marine mammal's offset crossline. In greater depths the crossline position becomes less important and exposure histories mainly depend on the animal's diving depth.

(7) A doubling of the shot interval approximately halves the cumulative acoustic impact and the exposure zone radii.

(8) The 1 G gun fired at intervals of 10 s produces the lowest, the 8 G-gun cluster fired at intervals of 15 s the highest cumulative acoustic impact.

(9) Exposure zone radii depend mainly on the air-gun configuration and are almost independent of the water depth, sound velocity profile and seafloor properties. In case of single shots radii can roughly be predicted from the source level using a spherical spreading law. In case of multiple shots radii increase with lower thresholds according to a cylindrical spreading law, and the source level and shot interval contribute to the intercept. Single shot radii computed from rms levels using a 200 ms window are ~7 dB higher than SEL radii computed from the total seismogram duration.

(10) Source directivities computed for the exact air-gun cluster geometries illustrate, that side lobes are generated above 300 Hz

Table 8. Radii, where the 0-p SPLs ($SPL_{0\text{-}p}$) of a single shot and the SELs of multiple shots (SEL_{cum}) fall below the thresholds, which according to the dual criterion define the onset of PTS in cetaceans and underwater pinnipeds.

			PTS (injury), cetaceans						PTS (injury), pinnipeds					
			230 dB[a] ($SPL_{0\text{-}p}$)			198 dB[b] (SEL_{cum})			218 dB[a] ($SPL_{0\text{-}p}$)			186 dB[b] (SEL_{cum})		
Air-gun configuration/model	ΔT (s)	R	r (m)	h_{max} (m)	z (m)	r (m)	h_{max} (m)	z (m)	r (m)	h_{max} (m)	z (m)	r (m)	h_{max} (m)	z (m)
1 G-gun (8.5 l)														
Semi-infinite *iso*-velocity model	10	0.2	25	25	5	25	25	5	25	25	5	25	25	5
Deep water *iso*-velocity model	10	0.2	25	25	5	25	25	5	25	25	5	25	25	5
Amundsen/Bellingshausen Sea 715	10	0.2	25	25	5	25	25	5	25	25	5	58	50	30
Weddell Sea 25	10	0.2	25	25	5	25	25	5	25	25	5	58	50	30
Shallow water *iso*-velocity model	10	0.2	25	25	5	25	25	5	25	25	5	25	25	5
Amundsen/Bellingshausen Sea 687	10	0.2	25	25	5	25	25	5	25	25	5	58	50	30
Weddell Sea 7	10	0.2	25	25	5	25	25	5	25	25	5	58	50	30
3 GI-gun cluster (7.4 l)														
Semi-infinite *iso*-velocity model	10	0.2	25	25	5	25	25	5	25	25	5	58	50	30
Deep water *iso*-velocity model	10	0.2	25	25	5	25	25	5	25	25	5	58	50	30
Amundsen/Bellingshausen Sea 715	10	0.2	25	25	5	25	25	5	25	25	5	58	50	30
Weddell Sea 25	10	0.2	25	25	5	25	25	5	25	25	5	58	50	30
Shallow water *iso*-velocity model	10	0.2	25	25	5	25	25	5	25	25	5	58	50	30
Amundsen/Bellingshausen Sea 687	10	0.2	25	25	5	25	25	5	25	25	5	58	50	30
Weddell Sea 7	10	0.2	25	25	5	25	25	5	25	25	5	58	50	30
8 G-gun cluster (68.2 l)														
Semi-infinite *iso*-velocity model	15	0.2	25	25	5	93	75	55	58	50	30	1383	1000	955
Deep water *iso*-velocity model	15	0.2	25	25	5	93	75	55	58	50	30	1453	1025	1030
Amundsen/Bellingshausen Sea 715	15	0.2	25	25	5	128	100	80	58	50	30	1736	1250	1205
Weddell Sea 25	15	0.2	25	25	5	128	100	80	58	50	30	1754	1275	1205
Shallow water *iso*-velocity model	15	0.2	25	25	5	93	75	55	58	50	30	1023	950	380
Amundsen/Bellingshausen Sea 687	15	0.2	25	25	5	128	100	80	58	50	30	1669	1625	380
Weddell Sea 7	15	0.2	25	25	5	128	100	80	58	50	30	2000	2000	30
Weddell Sea 25	15	0.1	25	25	5	128	100	80	58	50	30	1702	1250	1155
Weddell Sea 7	15	0.1	25	25	5	128	100	80	58	50	30	1070	1000	380
Weddell Sea 25	15	0.3	25	25	5	128	100	80	58	50	30	1913	1325	1380
Weddell Sea 7	15	0.3	25	25	5	114	100	55	58	50	30	2250	2250	30
Weddell Sea 25	15	0.4	25	25	5	128	100	80	58	50	30	1896	1375	1305
Weddell Sea 7	15	0.4	25	25	5	114	100	55	58	50	30	3700	3700	30
Semi-infinite *iso*-velocity model	30	0.2	25	25	5	58	50	30	58	50	30	746	525	530
Deep water *iso*-velocity model	30	0.2	25	25	5	58	50	30	58	50	30	728	525	505
Amundsen/Bellingshausen Sea 715	30	0.2	25	25	5	58	50	30	58	50	30	923	650	655
Weddell Sea 25	30	0.2	25	25	5	58	50	30	58	50	30	888	650	605
Shallow water *iso*-velocity model	30	0.2	25	25	5	58	50	30	58	50	30	634	525	355
Amundsen/Bellingshausen Sea 687	30	0.2	25	25	5	58	50	30	58	50	30	841	750	380
Weddell Sea 7	30	0.2	25	25	5	58	50	30	58	50	30	1023	950	380
Semi-infinite *iso*-velocity model	60	0.2	25	25	5	25	25	5	58	50	30	392	275	280
Deep water *iso*-velocity model	60	0.2	25	25	5	25	25	5	58	50	30	375	275	255
Amundsen/Bellingshausen Sea 715	60	0.2	25	25	5	25	25	5	58	50	30	429	325	280
Weddell Sea 25	60	0.2	25	25	5	25	25	5	58	50	30	413	325	255
Shallow water *iso*-velocity model	60	0.2	25	25	5	25	25	5	58	50	30	410	300	280
Amundsen/Bellingshausen Sea 687	60	0.2	25	25	5	25	25	5	58	50	30	468	375	280
Weddell Sea 7	60	0.2	25	25	5	25	25	5	58	50	30	503	400	305
8 G + 1 Bolt 1500 LL-gun cluster (100.9 l)														
Semi-infinite *iso*-velocity model	60	0.2	25	25	5	25	25	5	58	50	30	605	450	405
Deep water *iso*-velocity model	60	0.2	25	25	5	25	25	5	58	50	30	605	450	405
Amundsen/Bellingshausen Sea 715	60	0.2	25	25	5	25	25	5	58	50	30	730	550	480
Weddell Sea 25	60	0.2	25	25	5	25	25	5	58	50	30	799	575	555
Shallow water *iso*-velocity model	60	0.2	25	25	5	25	25	5	58	50	30	593	475	355
Amundsen/Bellingshausen Sea 687	60	0.2	25	25	5	25	25	5	58	50	30	753	650	380
Weddell Sea 7	60	0.2	25	25	5	25	25	5	58	50	30	796	700	380

Notes: r is the total radius between source and receiver computed from the maximum horizontal offset h_{max}, where the threshold is exceeded and the corresponding receiver depth z according to $r = (z^2 + h_{max}^2)^{1/2}$. The accuracy of h_{max} and z is equal to the spacing of the synthetic seismograms in the FD model, that is, 25 m. Values are rounded to their nearest integers. In contrast to the definition in Southall *et al.* (2007) all radii are derived from unweighted SPLs and SELs. ΔT = shot interval, R = normal incidence reflection coefficient at the seafloor.

[a]0-p SPL in dB re 1 μPa.

[b]SEL in dB re 1 μPa^{2}s.

Table 9. Radii, where the rms SPLs (SPL_{rms}) of a single shot fall below the thresholds, which according to the rms level criterion define the onset of Level A and Level B harassment in cetaceans and underwater pinnipeds.

			Level A, pinnipeds 190 dB[a] (SPL_{rms})			Level A, cetaceans 180 dB[a] (SPL_{rms})			Level B, pinnipeds 170 dB[a] (SPL_{rms})			Level B, cetaceans 160 dB[a] (SPL_{rms})		
Air-gun configuration/model	ΔT (s)	R	r (m)	h_{max} (m)	z (m)	r (m)	h_{max} (m)	z (m)	r (m)	h_{max} (m)	z (m)	r (m)	h_{max} (m)	z (m)
1 G-gun (8.5 l)														
Semi-infinite *iso*-velocity model	10	0.2	25	25	5	81	75	30	260	225	130	800	675	430
Deep water *iso*-velocity model	10	0.2	25	25	5	81	75	30	260	225	130	800	675	430
Amundsen/Bellingshausen Sea 715	10	0.2	25	25	5	81	75	30	248	225	105	819	725	380
Weddell Sea 25	10	0.2	25	25	5	81	75	30	294	250	155	819	725	380
Shallow water *iso*-velocity model	10	0.2	25	25	5	81	75	30	260	225	130	763	675	355
Amundsen/Bellingshausen Sea 687	10	0.2	25	25	5	81	75	30	294	250	155	841	750	380
Weddell Sea 7	10	0.2	25	25	5	81	75	30	282	250	130	863	775	380
3 GI-gun cluster (7.4 l)														
Semi-infinite *iso*-velocity model	10	0.2	25	25	5	114	100	55	282	250	130	974	800	555
Deep water *iso*-velocity model	10	0.2	25	25	5	114	100	55	282	250	130	974	800	555
Amundsen/Bellingshausen Sea 715	10	0.2	58	50	30	114	100	55	378	300	230	1050	875	580
Weddell Sea 25	10	0.2	58	50	30	114	100	55	363	300	205	1113	900	655
Shallow water *iso*-velocity model	10	0.2	25	25	5	114	100	55	282	250	130	807	725	355
Amundsen/Bellingshausen Sea 687	10	0.2	58	50	30	114	100	55	378	300	230	875	800	355
Weddell Sea 7	10	0.2	58	50	30	114	100	55	363	300	205	898	825	355
8 G-gun cluster (68.2 l)														
Semi-infinite *iso*-velocity model	15	0.2	239	200	130	703	575	405	2203	1775	1305	6737	5525	3855
Deep water *iso*-velocity model	15	0.2	239	200	130	703	575	405	2203	1775	1305	6088	5350	2905
Amundsen/Bellingshausen Sea 715	15	0.2	226	200	105	745	625	405	2468	1975	1480	5642	5225	2130
Weddell Sea 25	15	0.2	226	200	105	731	625	380	2488	2000	1480	5601	5200	2080
Shallow water *iso*-velocity model	15	0.2	239	200	130	676	575	355	1938	1900	380	5638	5625	380
Amundsen/Bellingshausen Sea 687	15	0.2	226	200	105	719	625	355	2625	2625	30	5986	5975	355
Weddell Sea 7	15	0.2	226	200	105	707	625	330	2375	2375	30	6060	6050	355
Weddell Sea 25	15	0.1	226	200	105	731	625	380	2488	2000	1480	5601	5200	2080
Weddell Sea 7	15	0.1	226	200	105	719	625	355	2110	2075	380	6636	6625	380
Weddell Sea 25	15	0.3	226	200	105	731	625	380	2488	2000	1480	5601	5200	2080
Weddell Sea 7	15	0.3	226	200	105	729	650	330	1982	1950	355	5861	5850	355
Weddell Sea 25	15	0.4	226	200	105	731	625	380	2488	2000	1480	6625	6025	2755
Weddell Sea 7	15	0.4	226	200	105	1023	950	380	1908	1875	355	5511	5500	355
8 G + 1 Bolt 1500 LL-gun cluster (100.9 l)														
Semi-infinite *iso*-velocity model	60	0.2	294	250	155	904	750	505	2963	2350	1805	8009	6950	3980
Deep water *iso*-velocity model	60	0.2	294	250	155	904	750	505	2963	2350	1805	7211	6600	2905
Amundsen/Bellingshausen Sea 715	60	0.2	329	275	180	994	825	555	3179	2600	1830	6287	5975	1955
Weddell Sea 25	60	0.2	316	275	155	981	825	530	3308	2650	1980	6231	5925	1930
Shallow water *iso*-velocity model	60	0.2	294	250	155	785	700	355	2179	2150	355	6435	6425	355
Amundsen/Bellingshausen Sea 687	60	0.2	329	275	180	819	750	330	2900	2900	30	7477	7475	155
Weddell Sea 7	60	0.2	316	275	155	852	775	355	2875	2875	30	7009	7000	355

Notes: r is the total radius between source and receiver computed from the maximum horizontal offset h_{max}, where the threshold is exceeded and the corresponding receiver depth z according to $r = (z^2 + h_{max}^2)^{1/2}$. The accuracy of h_{max} and z is equal to the spacing of the synthetic seismograms in the FD model, that is, 25 m. Values are rounded to their nearest integers. All radii are derived from unweighted rms SPLs by averaging over a window length of 200 ms. ΔT = shot interval, R = normal incidence reflection coefficient at the seafloor.
[a]Rms SPL in dB re 1 μPa.

with levels more than 30 dB below the spectral peak level of the main lobe. A comparison with the directivity of a point source shows, that the relative amount of energy between ∼100 and 300 Hz is slightly higher for the point source than for the air-gun clusters. Thus, a small portion of side lobe energy is neglected by the band limitation (0–256 Hz) of the FD modelling studies, but some additional energy is simultaneously introduced by the point source approximation, so that the exposure zone radii can be taken as upper limits.

(11) Estimations of the lower cut-off frequencies of the near-surface ducts yield, that in the Southern Ocean seismic frequencies higher than same tens of Hertz can already be trapped in the ducts due to their large thicknesses. That means the dominant portion of the seismic energy, which can be trapped in the near-surface ducts, is included in the band-limited modelling studies, so that no considerable effects on critical exposure zone radii are expected, if higher frequencies and side lobes would be included.

(12) All exposure zone radii are derived from the band-limited data without considering the frequency-selective M-weighting functions for different marine mammal hearing groups. Thus, all radii are upper limits, particularly for mid- and high-frequency cetaceans and pinnipeds.

ACKNOWLEDGMENTS

This study is a contribution to a risk assessment on the impact of seismic research surveys on marine mammals in the Antarctic Treaty area prepared by the Alfred-Wegener-Institute (AWI)

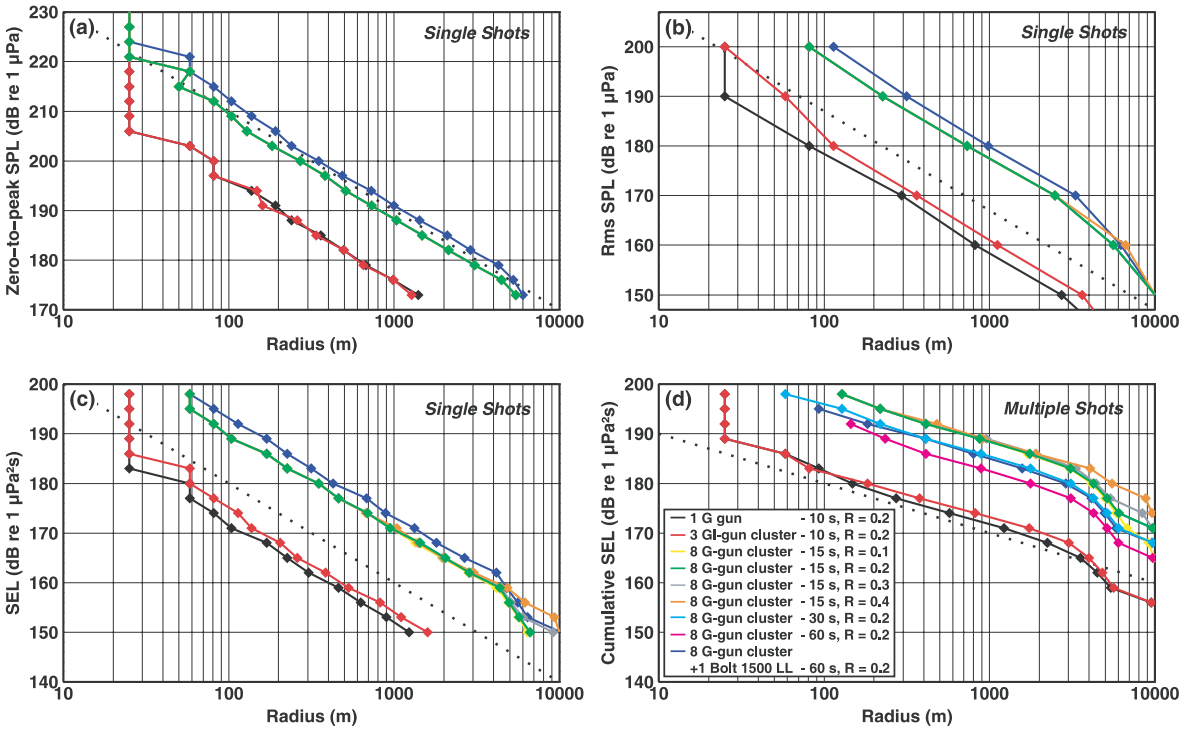

Figure 21. Deep water model for the Weddell Sea. Exposure zone radii for different thresholds and air-gun configurations (see legend for colours). (a) 0-p SPL thresholds of single shots, (b) rms SPL thresholds of single shots, (c) SEL thresholds of single shots, (d) cumulative SEL thresholds of multiple shots. Note, that the ordinate of the rms SPL thresholds is shifted by 7 dB compared to the ordinate of the SEL thresholds of single shots to facilitate their comparison. The dotted lines indicate a spherical 20 $\log_{10} r$ decay in the single shot diagrams and a cylindrical 10 $\log_{10} r$ decay in the multiple shots diagram. The exposure zone radii of the deep water Amundsen/Bellingshausen Sea model show very similar trends.

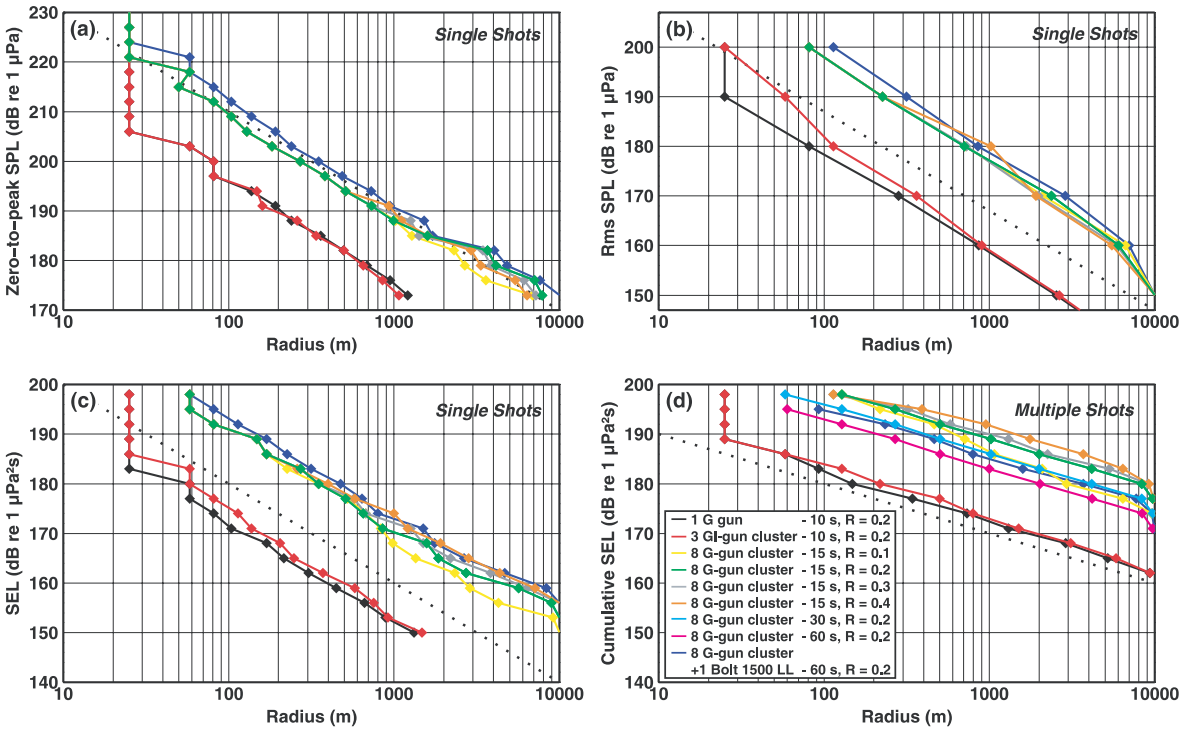

Figure 22. Shallow water model for the Weddell Sea. Exposure zone radii for different thresholds and air-gun configurations (see legend for colours). (a) 0-p SPL thresholds of single shots, (b) rms SPL thresholds of single shots, (c) SEL thresholds of single shots, (d) cumulative SEL thresholds of multiple shots. Note, that the ordinate of the rms SPL thresholds is shifted by 7 dB compared to the ordinate of the SEL thresholds of single shots to facilitate their comparison. The dotted lines indicate a spherical 20 $\log_{10} r$ decay in the single shot diagrams and a cylindrical 10 $\log r$ decay in the multiple shots diagram. The exposure zone radii of the shallow water Amundsen/Bellingshausen Sea model show very similar trends.

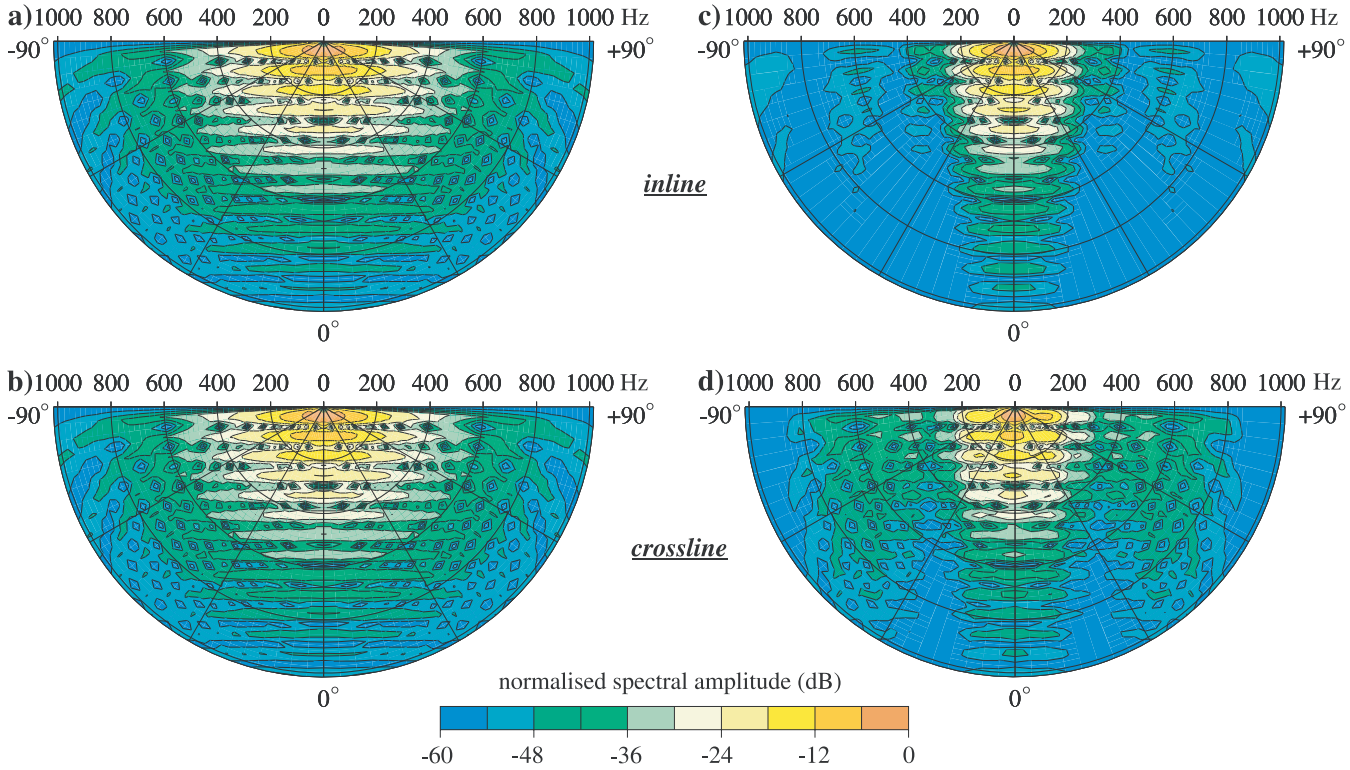

Figure 23. Comparison of the frequency-dependent directivities of the 1 G gun inline (a), the 1 G gun crossline (b), the 8 G + 1 Bolt 1500 LL gun cluster inline (c), the 8 G + 1 Bolt 1500 LL-gun cluster crossline (d) computed by the NUCLEUS^{TM} software for the exact cluster geometry, towing depths and pressures (Table 5). Frequencies are plotted along the radii. Angles are measured from the vertical. Spectral amplitudes are normalised to 0 dB for each air-gun configuration separately.

for the German Federal Environment Agency (UBA). We thank Olaf Boebel, Horst Bornemann, Elke Burkhardt, Karsten Gohl, Wilfried Jokat, Heinrich Miller and Christoph Ruholl for their helpful discussions on all acoustic, seismic, biological and legal aspects related to anthropogenic noise and marine mammals in the Antarctic Treaty area, Michael Schroeter and Chresten Wuebber for their support in using the NEC-SX8 of AWI's Scientific Computing Centre, and John Diebold for providing the opportunity to use the NUCLEUS^{TM} software during a stay at the Lamont Doherty Earth Observatory (LDEO). The helpful comments of two anonymous reviewers are also greatly acknowledged. Most of the figures were produced using the free software GMT (Wessel & Smith 1991). Seismogram sections were plotted with the Seismic Unix software package (Stockwell 1997).

REFERENCES

Blackman, D.K., de Groot-Hedlin, C., Harben, P., Sauter, A. & Orcutt, J.A., 2004. Testing low/very low frequency acoustic sources for basin-wide propagation in the Indian Ocean, *J. acoust. Soc. Am.,* **116,** 2057–2066.

Bohlen, T., 2002. Parallel 3-D viscoelastic finite difference seismic modelling, *Comput. Geosci.,* **28,** 887–899.

Bohlen, T., Kugler, S., Klein, G. & Theilen, F., 2004. 1.5D inversion of lateral variation of Scholte-wave dispersion, *Geophysics,* **69,** 330–344.

Breitzke, M., Boebel, O., El Naggar, S., Jokat, W. & Werner, B., 2008. Broadband calibration of marine seismic sources used by R/V *Polarstern* for academic research in polar regions, *Geophys. J. Int.,* **174,** 505–524.

Brekhovskikh, L.M. & Lysanov, Y.P., 2003. *Fundamentals of Ocean Acoustics,* Springer Verlag, New York.

Caldwell, J. & Dragoset, W., 2000. A brief overview of seismic air-gun arrays, *The Leading Edge,* **19,** 898–902.

Cerjan, C., Kosloff, D., Kosloff, R. & Reshef, M., 1985. A nonreflecting boundary condition for discrete acoustic and elastic wave equations, *Geophysics,* **50,** 705–708.

Collins, M.D., 1993. A split-step Padé solution for the parabolic equation method, *J. acoust. Soc. Am.,* **93,** 1736–1742.

Collins, M.D., 1999. The stabilized self-starter, *J. acoust. Soc. Am.,* **106,** 1724–1726.

D'Spain, G.L., D'Amico, A. & Fromm, D.M., 2006. Properties of underwater sound fields during some well documented beaked whale mass stranding events, *J. Cetacean Res. Manag.,* **7,** 223–238.

de Groot-Hedlin, C., Blackman, D.K. & Jenkins, C.S., 2009. Effects of variability associated with the Antarctic circumpolar current on sound propagation in the ocean, *Geophys. J. Int.,* **176,** 478–490.

DeRuiter, S.L., Tyack, P.L., Lin, Y.T., Newhall, A.E., Lynch, J.F. & Miller, P.J.O., 2006. Modelling acoustic propagation of airgun array pulses recorded on tagged sperm whales *(Physeter macrocephalus), J. acoust. Soc. Am.,* **120,** 4100–4114.

Dowdeswell, J.A., O'Cofaigh, C., Noormets, R., Larter, R.D., Hillenbrand, C.D., Benetti, S., Evans, J. & Pudsey, C.J., 2008. A major trough-mouth fan on the continental margin of the Bellingshausen Sea, West Antarctica: The Belgica Fan, *Mar. Geol.,* **252,** 129–140.

Dragoset, W.H., 2000. Introduction to air guns and air-gun arrays, *The Leading Edge,* **19,** 892–897.

Erbe, C. & King, A., 2009. Modeling cumulative sound exposure around marine seismic surveys, *J. acoust. Soc. Am.,* **125,** 2443–2451.

Etter, P.C., 2003. *Underwater Acoustic Modeling and Simulation,* Spon Press, London.

Fahrbach, E., Rohardt, G. & Sieger, R., 2007. *25 Years of Polarstern Hydrography (1982 – 2007),* WDC-MARE Reports, 0005, Alfred Wegener Institute for Polar and Marine Research (AWI), Bremerhaven and Center for Marine Environmental Sciences (MARUM), Bremen.

Gisiner, R., Harper, S., Livingston, E. & Simmen, J., 2006. Effects of sound on the marine environment (ESME): An underwater noise risk model, *IEEE J. Ocean. Eng.,* **31,** 4–7.

Hamilton, E.L., 1980. Geoacoustic modeling of the sea floor, *J. acoust. Soc. Am.,* **68,** 1313–1340.

Houser, D.S., 2006. A method for modeling marine mammal movement and behavior for environmental impact assessment, *IEEE J. Ocean. Eng.,* **31,** 76–81.

Jensen, F.B., Kuperman, W.A., Porter, M.B. & Schmidt, H., 2000. *Computational Ocean Acoustics,* Springer Verlag, New York.

Jokat, W., Buratsev, V.Y. & Miller, H., 1995. Marine seismic profiling in ice covered regions, *Polarforschung,* **64,** 9–17.

Kugler, S., Bohlen, T., Bussat, S. & Klein, G., 2005. Variability of Scholte-wave dispersion in shallow-water marine sediments, *J. Environ. Eng. Geophys.,* **10,** 203–218.

Kugler, S., Bohlen, T., Forbriger, T., Bussat, S. & Klein, G., 2007. Scholte-wave tomography for shallow-water marine sediments, *Geophys. J. Int.,* **168,** 551–570.

Kuhn, G. & Weber, M., 1993. Acoustical characterization of sediments by Parasound and 3.5-kHz systems: Related sedimentary processes on the southeastern Weddell Sea continental slope, Antarctica, *Mar. Geol.,* **113,** 201–217.

Landrø, M., 1992. Modelling of GI gun signatures, *Geophys. Prospect.,* **40,** 721–747.

Landrø, M., Mittet, R. & Sollie, R., 1993. Implementing measured source signatures in a coarse-grid, finite-difference modeling scheme, *Geophysics,* **59,** 1852–1860.

Laws, R.M., Hatton, L. & Haartsen, M., 1990. Computer modelling of clustered airguns, *First Break,* **8,** 331–338.

Levander, A.R., 1988. Fourth-order finite-difference P-SV seismograms, *Geophysics,* **53,** 1425–1436.

LGL Ltd. 2008. *Environmental assessment of a marine geophysical survey by the R/V Marcus G. Langseth in Southeast Asia, March-July 2009,* LGL Report, TA4553–1, LGL Ltd., environmental research associates, King City, Ontario L7B 1A6.

Linder, C.A. & Gawarkiewicz, G.G., 2006. Oceanographic and sound speed fields for the ESME workbench, *IEEE J. Ocean. Eng.,* **31,** 22–32.

Lurton, X., 2002. *An Introduction to Underwater Acoustics,* 347 pp., Springer Verlag and Praxis Publishing Ltd., Chichester.

Lynch, J.F. *et al*. 2006. Consideration of fine-scale coastal oceanography and 3-D acoustics effects for the ESME sound exposure model, *IEEE J. Ocean. Eng.,* **31,** 33–48.

Madsen, P.T., 2005. Marine mammals and noise: Problems with root mean square sound pressure levels for transients, *J. acoust. Soc. Am.,* **117,** 3952–3957.

Madsen, P.T., Johnson, M., Miller, P.J.O., Aguilar Soto, N., Lynch, J. & Tyack, P., 2006. Quantitative measures of air-gun pulses recorded on sperm whales (*Physeter macrocephalus*) using acoustic tags during controlled exposure experiments, *J. acoust. Soc. Am.,* **120,** 2366–2379.

Melles, M. & Kuhn, G., 1993. Sub-bottom profiling and sedimentological studies in the southern Weddell Sea, Antarctica: evidence for large-scale erosional/depositional processes, *Deep-Sea Res. I,* **40,** 739–760.

Michels, K.H., Kuhn, G., Hillenbrand, C.D., Diekmann, B., Fütterer, D.K., Grobe, H. & Uenzelmann-Neben, G., 2002. The southern Weddell Sea: combined contourite-turbidite sedimentation at the southeastern margin of the Weddell Gyre, in *Deep-water Contourite Systems: Modern Drifts and Ancient Series, Seismic and Sedimentary Characteristics,* pp. 305–323, eds Stow, D.A.V. *et al*., Geological Society, London, Memoirs, The Geological Society of London.

National Marine Fisheries Service, 2008. Incidental takes of marine mammals during specified activities; marine geophysical survey in Southeast Asia, March-July 2009, *Federal Register,* **73,** 78294–78317.

Nitsche, F.O., Cunningham, A.P, Larter, R.D. & Gohl, K., 2000. Geometry and development of glacial continental margin depositional systems in the Bellingshausen Sea, *Mar. Geol.,* **162,** 277–302.

Porter, M.B. & Jensen, F.B., 1993. Anomalous parabolic equation results for propagation in leaky surface ducts, *J. acoust. Soc. Am.,* **94,** 1510–1516.

Ricker, N., 1953. The form and laws of propagation of seismic wavelets, *Geophysics,* **18,** 10–40.

Scheuer, C., Gohl, K., Larter, R.D., Rebesco, M. & Udintsev, G., 2006a. Variability in Cenozoic sedimentation along the continental rise of the Bellingshausen Sea, West Antarctica, *Mar. Geol.,* **227,** 279–298.

Scheuer, C., Gohl, K. & Udintsev, G., 2006b. Bottom-current control on sedimentation in the western Bellingshausen Sea, West Antarctica, *Geo-Mar. Lett.,* **26,** 90–101.

Shaffer, S.A. & Costa, D.P., 2006. A database for the study of marine mammal behavior: Gap analysis, data standardization, and future directions, *IEEE J. Ocean. Eng.,* **31,** 82–86.

Shyu, H.J. & Hillson, R., 2006. A Software Workbench for estimating the effects of cumulative sound exposure in marine mammals, *IEEE J. Ocean. Eng.,* **31,** 8–21.

Siderius, M. & Porter, M.B., 2006. Modeling techniques for marine-mammal risk assessment, *IEEE J. Ocean. Eng.,* **31,** 49–60.

Sidorovskaia, N.A., 2004. Systematic studies of pulse propagation in ducted oceanic waveguides in normal mode representation, *Eur. Phys. J. appl. Phys.,* **25,** 113–131.

Southall, B.L. *et al*., 2007. Marine mammal noise exposure criteria: Initial scientific recommendations, *Aquat. Mammals,* **33,** 411–521.

Stockwell, J.W., 1997. Free software in education: A case study with CWP/SU: Seismic Un∗x, *Leading Edge,* **16,** 1045–1049.

Tashmukhambetov, A.M., Ioup, G.E., Ioup, J.W., Sidorovskaia, N.A. & Newcomb, J.J., 2008. Three-dimensional seismic array characterization study: Experiment and modeling, *J. acoust. Soc. Am.,* **123,** 4094–4108.

Tolstoy, M., Diebold, J., Doermann, L., Nooner, S., Webb, S.C., Bohnenstiel, D.R., Crone, T.J. & Holmes, R.C., 2009. Broadband calibration of R/V *Marcus Langseth* four-string seismic sources, *Geochem. Geophys. Geosyst.,* **10,** Q08011, doi: 08010.01029/02009GC002451.

Tolstoy, M., Diebold, J.B., Webb, S.C., Bohnenstiel, D.R., Chapp, E., Holmes, R.C. & Rawson, M., 2004. Broadband calibration of R/V *Ewing* seismic sources, *Geophys. Res. Lett.,* **31,** L14310, doi:14310.11029/12004GL020234.

Urick, R.J., 1983. *Principles of Underwater Sound,* 3rd edn, 423 pp., McGraw Hill, New York.

Virieux, J., 1986. P-SV wave propgation in heterogeneous media: velocity-stress finite-difference method, *Geophysics,* **51,** 889–901.

Wardell, N., Childs, J.R. & Cooper, A.K., 2007. Advances through collaboration: sharing seismic reflection data via the Antarctic Seismic Data Library System for Cooperative Research (SDLS), in *Antarctica: A Keystone in a Changing World – Online Proceedings of the 10th ISAES,* pp. 4, eds Cooper, A.K. *et al*., USGS Open-File Report 2007-1047.

Wessel, P. & Smith, W.H.F., 1991. Free software helps map and display data, *EOS, Trans. Am. geophys. Un.,* **72,** 441 and 445–446.

Williams, C.M., Stephen, R.A. & Smith, D.K., 2006. Hydroacoustic events located at the intersection of the Atlantis (30°N) and Kane (23°40′N) Transform Faults with the Mid-Atlantic Ridge, *Geochem. Geophys. Geosyst.,* **7,** Q060, doi:10.1029/2005GC001127.

Ziolkowski, A., 1970. A method for calculating the output pressure waveform from an air gun, *Geophys. J. R. astr. Soc.,* **21,** 137–161.

Ziolkowski, A.M., Parkes, G., Hatton, L. & Haugland, T., 1982. The signature of an air gun array: Computation from near-field measurements including interactions, *Geophysics,* **47,** 1413–1421.

APPENDIX

A.1 Marine mammal hearing groups and frequency-selective M-weighting functions

To describe the hearing sensitivities of different species of marine mammals analytically, Southall *et al.* (2007) defined five groups of marine mammals with similar hearing and developed frequency-selective weighting functions (called 'M-weighting' functions) to describe their auditory bandwidth. The five groups are: (1) mysticetes (baleen whales), designated as 'low-frequency cetaceans',

Table A1. Marine mammal hearing groups and their estimated lower and upper frequency hearing cut-offs used in the M-weighting functions.

Functional hearing group	Examples	Low-cut frequency (Hz)	High-cut frequency (kHz)
Low-frequency cetaceans	Baleen whales	7	22
Mid-frequency cetaceans	Toothed whales	150	160
High-frequency cetaceans	Porpoises, river dolphins	200	180
Pinnipeds in water	Seals, sea lions, walruses	75	75
Pinnipeds in air	Seals, sea lions, walruses	75	30

Note: After Southall *et al.* (2007).

(2) some odontocetes (toothed whales), designated as 'mid-frequency cetaceans', (3) odontocetes specialized for using high frequencies (e.g. porpoises, river dolphins), designated as 'high-frequency cetaceans', (4) pinnipeds listening in water (e.g. seals, sea lions, walruses) and (5) pinnipeds listening in air. The frequency-dependent M-weighting functions are given by (Southall *et al.* 2007)

$$M(f) = 20 \log_{10} \frac{R(f)}{\max\{|R(f)|\}}, \tag{A1}$$

where

$$R(f) = \frac{f_{\text{high}}^2 f^2}{\left(f_{\text{high}}^2 + f^2\right)\left(f_{\text{low}}^2 + f^2\right)}. \tag{A2}$$

The frequencies f_{low} and f_{high} define the estimated lower and upper hearing limits for each of the five marine mammal hearing groups and are listed in Table A1. The corresponding M-weighting functions are displayed in Fig. A1. They indicate, that the estimated hearing sensitivities roll off by 12 dB/octave below and above the cut-off frequencies. The seismic bandwidth with dominant frequencies around 100 Hz is perceived with almost no attenuation only by low-frequency cetaceans. The auditory systems of mid- and high-frequency cetaceans and pinnipeds filter parts of the seismic energy

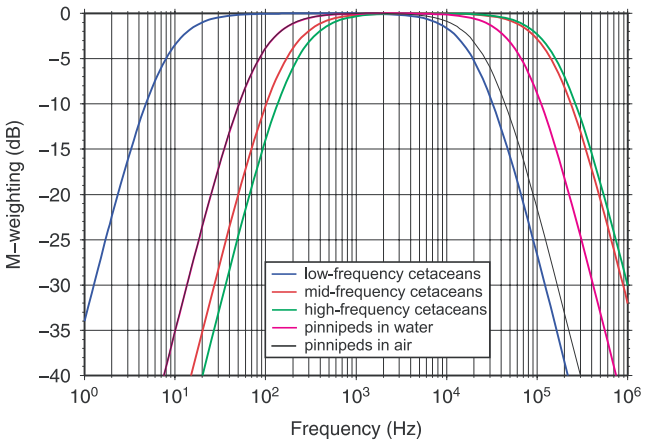

Figure A1. M-weighting functions for the five marine mammals hearing groups defined by Southall *et al.* (2007).

out, so that the actually heard levels are lower than the broad-band levels shown in this paper. Consequently, for mid- and high-frequency cetaceans and pinnipeds all derived exposure zone radii are by far upper limits.